

Galactic Bulge Microlensing Optical Depth from EROS-2[★]

C. Hamadache¹, L. Le Guillou^{1**}, P. Tisserand^{1***}, C. Afonso^{1†}, J.N. Albert², J. Andersen⁵, R. Ansari²,
É. Aubourg¹, P. Barette¹, J.P. Beaulieu³, X. Charlot¹, C. Coutures^{1,3}, R. Ferlet³, P. Fouqué^{7,8}, J.F. Glicenstein¹,
B. Goldman^{1‡}, A. Gould⁶, D. Graff^{6§}, M. Gros¹, J. Haissinski², J. de Kat¹, É. Lesquoy^{1,3}, C. Loup³, C. Magneville¹,
J.B. Marquette³, É. Maurice⁴, A. Maury^{8¶}, A. Milsztajn¹, M. Moniez², N. Palanque-Delabrouille¹, O. Perdureau²,
Y.R. Rahal², J. Rich¹, M. Spiro¹, A. Vidal-Madjar³, L. Vigroux^{1,3}, S. Zylberajch¹
The EROS-2 collaboration

¹ CEA, DSM, DAPNIA, Centre d'Études de Saclay, 91191 Gif-sur-Yvette Cedex, France

² Laboratoire de l'Accélérateur Linéaire, IN2P3 CNRS, Université de Paris-Sud, 91405 Orsay Cedex, France

³ Institut d'Astrophysique de Paris, UMR7095 CNRS, Université Pierre & Marie Curie, 98 bis Boulevard Arago, 75014 Paris, France

⁴ Observatoire de Marseille, 2 place Le Verrier, 13248 Marseille Cedex 04, France

⁵ The Niels Bohr Institute, Copenhagen University, Juliane Maries Vej 30, DK2100 Copenhagen, Denmark

⁶ Department of Astronomy, Ohio State University, Columbus, OH 43210, U.S.A.

⁷ Observatoire Midi-Pyrénées, Laboratoire d'Astrophysique (UMR 5572), 14 av. E. Belin, 31400 Toulouse, France

⁸ European Southern Observatory (ESO), Casilla 19001, Santiago 19, Chile

Received;accepted

Abstract. We present a new EROS-2 measurement of the microlensing optical depth toward the Galactic Bulge. Light curves of 5.6×10^6 clump-giant stars distributed over 66 deg^2 of the Bulge were monitored during seven Bulge seasons. 120 events were found with apparent amplifications greater than 1.6 and Einstein radius crossing times in the range $5 \text{ d} < t_E < 400 \text{ d}$. This is the largest existing sample of clump-giant events and the first to include northern Galactic fields. In the Galactic latitude range $1.4^\circ < |b| < 7.0^\circ$, we find $\tau/10^{-6} = (1.62 \pm 0.23) \exp[-a(|b| - 3 \text{ deg})]$ with $a = (0.43 \pm 0.16) \text{ deg}^{-1}$. These results are in good agreement with our previous measurement, with recent measurements of the MACHO and OGLE-II groups, and with predictions of Bulge models.

Key words. Galaxy:bar - Galaxy:stellar contents - Galaxy:structure - Cosmology:gravitational lensing

1. Introduction

Gravitational microlensing of stars is an important tool for constraining the quantity and characteristics of faint compact objects between the stars and the observer. In microlensing

events, the lensing object passes near the line of sight towards the background star, causing a transient magnification of the star's primary image as well as creating a secondary image. At Galactic scales, neither the image separation nor the image size are normally resolvable, so the only easily observable effect during a microlensing event is an apparent transient amplification of the star's flux. The characteristic timescale giving the effective duration of the amplification is proportional to the square root of the lens mass and inversely proportional to the transverse velocity. For Galactic stellar lenses, the timescales are on the order of a few weeks.

Microlensing searches were originally proposed (Paczynski 1986) as a tool for detecting dark matter in galactic halos. Searches for the lensing of stars in the Magellanic Clouds by the MACHO (Alcock et al. 2000b) and EROS-2 (Afonso et al. 2003a; Tisserand et al. 2006) projects have placed constraints on the fraction of the Milky Way halo that can be comprised of faint compact objects. Searches for objects in the halo of M31 are also being performed with candidate events reported by the VATT-Columbia (Uglesich et al. 2004),

[★] Based on observations made with the MARLY telescope at the European Southern Observatory, La Silla, Chile.

^{**} Now at Instituut voor Sterrenkunde, Celestijnenlaan 200 B, B-3001 Leuven, Belgium

^{***} Now at Research School of Astronomy and Astrophysics, Australian National University, Mount Stromlo Obs., Cotter Rd., Weston, ACT 2611, Australia

[†] Now at Max-Planck-Institut für Astronomie, Königstuhl 17, D-69117 Heidelberg, Germany

[‡] Now at Max-Planck-Institut für Astronomie, Königstuhl 17, D-69117 Heidelberg, Germany

[§] Now at Division of Medical Imaging Physics, Johns Hopkins University Baltimore, MD 21287-0859, USA

[¶] Now at San Pedro de Atacama Celestial Exploration, Casilla 21, San Pedro de Atacama, Chile

WeCAPP (Riffeser et al. 2003), AGAPE (Calchi Novati et al. 2005), MEGA (de Jong et al. 2006) and Nainital (Joshi et al. 2005) collaborations. The AGAPE and MEGA collaborations presented efficiency calculations allowing them to constrain the content of the M31 and Milky Way halos.

Microlensing has also been used as a tool to investigate compact objects in the visible regions of the Milky Way. Besides the Galactic Bulge that is the subject of this paper, microlensing of stars in the spiral arms of the Galaxy has also been studied (Derue et al. 2001).

Microlensing surveys toward the Galactic Bulge were first proposed (Paczynski 1991; Griest 1991) as a probe of ordinary stars in the Galactic Disk, though it was soon realized (Kiraga & Paczynski 1994) that lensing by stars in the Bulge itself is of comparable importance. The optical depth, i.e. the probability that at a given time a star at a distance D_s is amplified by more than a factor 1.34 is

$$\tau = \frac{4\pi G D_s^2}{c^2} \int_0^1 \rho(x)x(1-x)dx, \quad (1)$$

where ρ is the mass density of lenses and $x = D_l/D_s$ is the ratio between the lens and source distances. Very qualitatively, the integral for the Disk contribution to the optical depth is

$$\tau_{\text{disk}} \sim \frac{GM_{\text{disk}}}{c^2 h_{\text{disk}}}, \quad (2)$$

where M_{disk} and h_{disk} are the total mass and scale height of the Disk lensing population. Lenses in the Bulge are near the source star so the Bulge contribution is

$$\tau_{\text{bulge}} \sim \frac{GM_{\text{bulge}}}{c^2 R_{\text{bulge}}} \sim \frac{G\rho_{\text{bulge}}R_{\text{bulge}}^2}{c^2}, \quad (3)$$

where M_{bulge} , ρ_{bulge} and R_{bulge} are the mass, density and line of sight thickness of the Bulge lensing population. For Bulge stars near the direction of the Baade window ($l = 1^\circ$, $b = -3.9^\circ$), the most recent calculations (Evans & Belokurov 2002; Bissantz & Gerhard 2002; Han & Gould 2003; Wood and Mao 2005) give total optical depths in the range $1 < \tau/10^{-6} < 2$, with about 60% of the rate being due to lensing by Bulge stars and the remainder by Disk stars. The expected optical depth naturally has a strong dependence on the Galactic latitude, b , falling typically from $\tau \sim 5 \times 10^{-6}$ at ($l \sim 0$, $|b| = 1^\circ$) to $\tau \sim 5 \times 10^{-7}$ at ($l \sim 0$, $|b| = 6^\circ$).

The first measurements of the optical depth towards the Galactic Bulge by the OGLE collaboration (Udalski et al. 1994b, 2000; Woźniak et al. 2001), the MACHO collaboration (Alcock et al. 1997, 2000a) and the MOA collaboration (Sumi et al. 2003) yielded optical depths significantly higher than these estimates, suggesting that a fundamental revision of Galactic models might be necessary (Binney et al. 2000). However, the interpretation of the first results was difficult because of two effects. First, stars in the direction of the Galactic Bulge are not necessarily located in the Bulge itself so foreground and background contamination must be taken into account. Second, and more importantly, photometry of the numerous faint stars in the crowded Galactic Bulge fields is complicated by “blending” where the reconstructed stellar flux receives contributions from more than one star. This makes the

effective number of monitored stars greater than the number of cataloged stars and generates a complicated relationship between real and reconstructed amplifications.

These problems can be largely avoided by considering only microlensing of clump giant stars. Such stars are identified by their well-defined position in the color-magnitude diagram. This position ensures that they are most likely in the Galactic Bulge. Their large flux also makes blending problems relatively unimportant.

The first published optical depth using clump giants was based on only 13 events observed by the MACHO group (Alcock et al. 1997). The optical depth, $3.9_{-1.2}^{+1.8} \times 10^{-6}$ at $\langle l, b \rangle = (2.55^\circ, -3.64^\circ)$, was still considerably higher than expectations. Since then, measurements using clump giants have tended to give results in better agreement with models. Based on 16 events, the EROS-2 collaboration (Afonso et al. 2003b) gave an optical depth of $0.94 \pm 0.29 \times 10^{-6}$ at $\langle l, b \rangle = (2.5^\circ, -4.0^\circ)$. The MACHO group (Popowski et al. 2005) recently presented their results using 62 events with clump giant sources. Their optical depth is $\tau = 2.17_{-0.38}^{+0.47} \times 10^{-6}$ at $\langle l, b \rangle = (1.5^\circ, -2.68^\circ)$, in good agreement with calculations and with their earlier preliminary results (Popowski et al. 2000). The OGLE-II group (Sumi et al. 2006) recently used 33 events to obtain $\tau = 2.55_{-0.46}^{+0.57} \times 10^{-6}$ at $\langle l, b \rangle = (1.16^\circ, -2.75^\circ)$, again in agreement with models.

In this paper we present a measurement of the optical depth for microlensing toward the Galactic Bulge based on the totality of the EROS-2 clump-giant data. More details on this analysis can be found in Hamadache (2004). The 120 events used comprise the largest sample of clump-giant events studied to date. Section 2 describes the data collection and processing required to produce the light curves. Section 3 describes the definition of the clump-giant sample to be used to measure the optical depth. Section 4 lists the criteria used to isolate a sample of microlensing candidates. Section 5 describes the calculation of the detection efficiency, the optical depth and the timescale distribution. Section 6 discusses the possibility that stellar blending may affect the results. Finally, Section 7 compares our results with those of other groups and with the predictions of Galactic models.

2. Data

The data were acquired by EROS-2 with the 1 m MARLY telescope at La Silla, Chile. The imaging was done simultaneously by two cameras, using a dichroic beam-splitter (Bauer et al. 1997). Each camera was composed of a mosaic of eight 2048×2048 pixel LORAL CCDs, with a pixel size of $0''.6$ yielding a field of $0.7^\circ(\alpha) \times 1.4^\circ(\delta)$. Each camera observed through one of two non-standard, broadband filters, R_{eros} and B_{eros} . The filter R_{eros} covers the range 620-920 nm and has a mean wavelength near that of Cousins I , while B_{eros} covers the range 420-720 nm and has a mean wavelength between Johnson/Cousins V and R . The photometric calibration was obtained directly for 20% of our fields by matching our star cata-

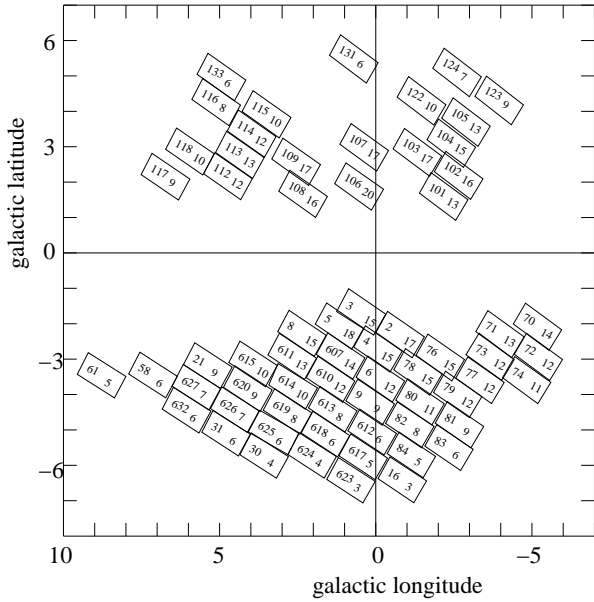


Fig. 1. Map of the EROS-2 Bulge fields in Galactic coordinates. A total of 66 fields were monitored. The first number in each field is the field number and the second is the number of clump giants in the field divided by 10^4 . The field 121 with 4×10^4 clump giants is outside the plot at $(l, b) = (11.5, 2.5)$.

logues with those of the OGLE-II collaboration (Udalski et al. 2002). To a precision of ~ 0.1 mag, we find

$$R_{\text{eros}} = I_{\text{ogle}}, \quad B_{\text{eros}} = V_{\text{ogle}} - 0.4(V - I)_{\text{ogle}}. \quad (4)$$

The calibration is sufficiently uniform that it can be extended with confidence to the remaining fields. We note, however, that none of our conclusions depend on the calibration precision.

The observations reported here concern 66 fields, monitored between July 1996 and October 2002. Figure 1 shows the location of the 66 fields in Galactic coordinates, (l, b) . Twenty-two of the fields are in the north ($b > 0$) and 44 in the south. The corresponding data set contains 6×10^7 pairs of light curves, of which 5.6×10^6 are Bulge clump giants that we use in the present analysis.

The fields are observable at La Silla from mid-February to mid-October. An average of one point every four nights was taken for each field during the observing season though the sampling frequency occasionally reached more than one point per night at mid-season when the Galactic Bulge is observable throughout the night.

The image photometry was performed with software specifically designed for crowded fields, PEIDA (Photométrie et Étude d’Images Destinées à l’Astrophysique) (Ansari 1996). The first step consisted of creating reference images for each of the 2112 subfields of size $\sim 0.035 \text{ deg}^2$, i.e. one quarter of a CCD. A reference image was constructed by adding 15 high-quality images of the subfield. Star catalogs for each subfield were established using the reference image. Photometry on individual images was then performed by imposing the stellar positions found on the reference image.

A first estimate of the uncertainty of individual flux measurements is that due to the photometric fit taking into ac-

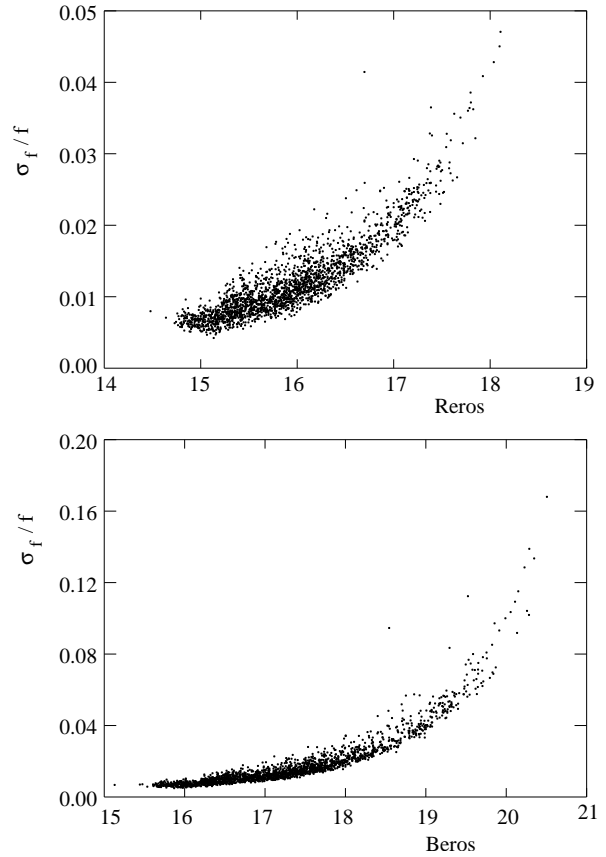


Fig. 2. The dispersion, σ/f_{base} , of clump-giant light curves about the base flux as a function of R_{eros} and of B_{eros} . Each point represents the median dispersion of clump giants for one subfield consisting of a CCD-quadrant.

count only photon counting statistics. This clearly underestimates the uncertainty since it ignores other contributions important in crowded field photometry, e.g. imperfect knowledge of the point-spread-function (PSF). The factor by which the uncertainties must be increased is determined by comparing individual flux measurements with the flux measurements of the same star on the reference image. The fit errors are increased by a magnitude and image dependent (but star independent) factor, chosen so that for each image the distribution of the difference between flux and reference flux is consistent with that expected from the renormalized flux uncertainties. By construction, this procedure yields, for most stars, a χ^2 per degree of freedom near unity for a fit to a time-independent flux.

The uncertainties on flux measurements are reflected in the dispersions of light curves about the baseline flux (estimated from the mode of the flux). Figure 2 shows, for each subfield, the median dispersion for clump giants in the two colors. The photometric precision is typically 2% but degrades considerably for B_{eros} in highly absorbed fields. We will be concerned only with microlensing apparent amplification factors > 1.6 so the precision in most fields is sufficiently good to yield high quality light curves in both colors. The 20% of the microlensing candidates with the lowest quality light curves were also photometered with our differential photometry package (Le Guillou 2004) so as to confirm their microlensing origin.

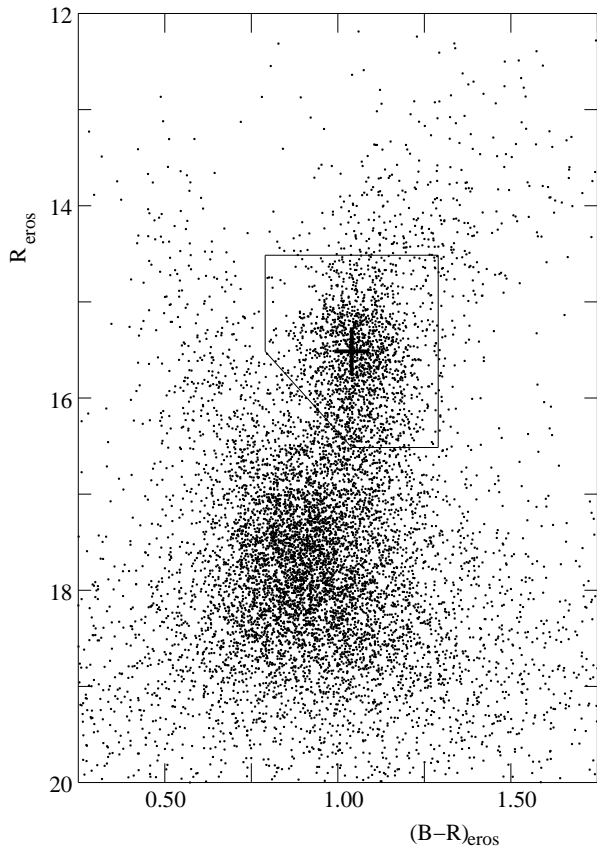


Fig. 3. A typical color-magnitude diagram of a subfield (field 610, CCD 4 quadrant 2). The cross shows the fitted center of the clump and the thin lines show the cuts defining the clump giants used in this analysis.

Examples of light curves containing microlensing events are shown in Figs. 21-23.

3. Clump giant selection

The sample of clump-giants to be studied was selected using the color-magnitude diagrams for each CCD-quadrant subfield. Figure 3 shows a diagram of a typical subfield. The center of the clump was determined by modeling the density of stars in color-magnitude space as a power law representing a smooth background plus a Gaussian representing the clump. The Gaussian had the form

$$\text{density} \propto \exp\left[-\frac{((B-R)_{\text{eros}} - \alpha)^2}{2\sigma_\alpha^2}\right] \times \exp\left[-\frac{(R_{\text{eros}} + 1.9(B-R)_{\text{eros}} - \beta)^2}{2\sigma_\beta^2}\right]$$

where α (σ_α) and β (σ_β) are the desired clump centers (widths) in the space defined by $(B-R)_{\text{eros}}$ and the reddening-free magnitude $R_{\text{eros}} + 1.9(B-R)_{\text{eros}}$. The dereddened magnitude is used so as to be relatively insensitive to variable reddening across the subfields.

Figure 4a shows the fitted R_{eros} of the clump center as a function of the fitted $(B-R)_{\text{eros}}$ of the clump center. The distribution follows the expected reddening law indicating that

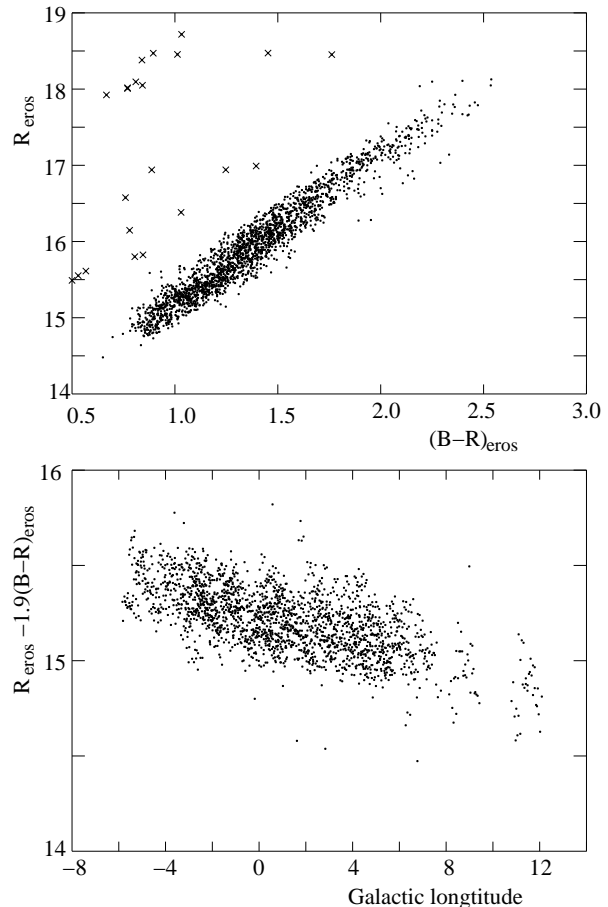


Fig. 4. The top panel shows R_{eros} of the clump center vs $B_{\text{eros}} - R_{\text{eros}}$ of the clump for the 2109 subfields (CCD quadrants). (Three quadrants were not reconstructed.) The distribution follows the expected reddening law. Quadrants marked with a \times were eliminated from further consideration. The bottom panel shows the dereddened magnitude as a function of Galactic longitude. The increasing flux with longitude is believed to be due to the bar structure since stars with $l < 0$ are farther than stars with $l > 0$.

variations of clump position are due to differential reddening. The 46 subfields that are outliers in this plot are excluded from further consideration leaving 2063 subfields. All 2063 color-magnitude diagrams were visually inspected to ensure that reasonable values for the clump position were found. We note that, in spite of the large variation of clump position, the clump is visually distinct in each of the 2063 diagrams. The variations of clump position lead to varying photometric precisions (Figure 2) but this is taken into account in the microlensing detection efficiency (Section 5).

Figure 4b shows the dereddened clump magnitude as a function of Galactic longitude, l . The longitude dependence is believed to be caused by the bar structure of the Bulge where stars with $l > 0$ are brighter than stars with $l < 0$ because they are nearer (Stanek et al. 1994). The 0.38 mag difference over 12° in longitude corresponds to a bar orientation of $49^\circ \pm 8^\circ$ with respect to the line of sight to the Galactic Center. This angle is in agreement with the original OGLE-

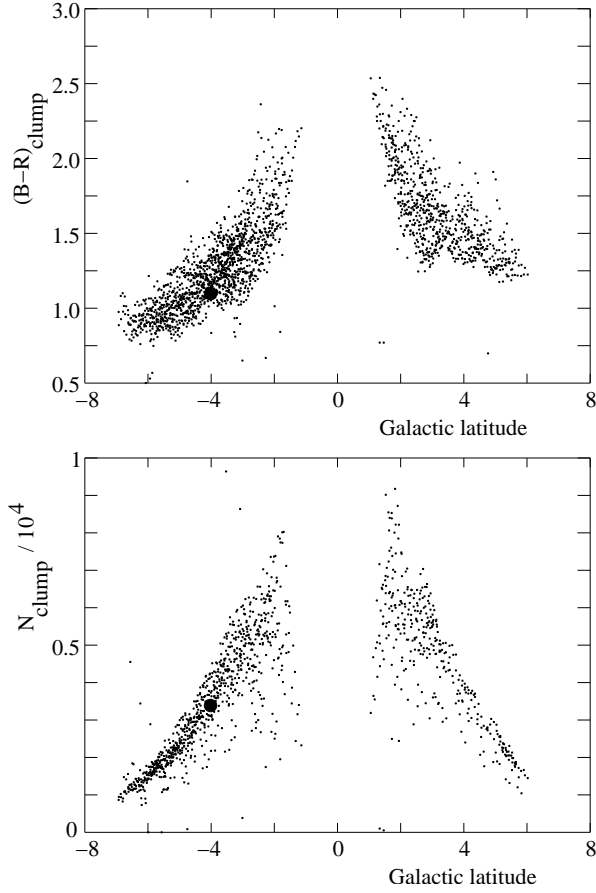


Fig. 5. The mean clump color (top panel) and the number of clump giants per CCD-quadrant (bottom panel) as a function of Galactic latitude for the longitude range $-3^\circ < \ell < 3^\circ$. The number of giants is symmetric about $b = 0$ while northern fields are more reddened than southern fields. The large dot marks the position of the subfield containing the Baade Window.

I results (Stanek et al. 1994) and with the recent infrared star counts from GLIMPSE (Benjamin et al. 2005).

Figure 5a shows the clump color as a function of Galactic latitude. The northern fields are more absorbed and reddened than the southern fields.

The cuts used to define our sample of clump giants, illustrated in Figure 3, are

$$|R - R_{\text{clump}}| < 1, \quad (5)$$

$$|(B - R) - (B - R)_{\text{clump}}| < 0.25, \quad (6)$$

$$R - R_{\text{clump}} > -4.[(B - R) - (B - R)_{\text{clump}}] - 1, \quad (7)$$

where R_{clump} and $(B - R)_{\text{clump}}$ define the clump center. The number of clump giants as a function of Galactic latitude is shown in Figure 5b. As expected, the number falls rapidly with increasing distance from the Galactic equator. In spite of the difference in absorption between northern and southern fields, there is no obvious asymmetry between counts of northern and southern clump giants, as expected.

4. Event Selection

After the production of the light curves, microlensing candidates among the 5.6×10^6 clump giants were found by the procedures described in this section. After elimination of images with instrumental problems or poor seeing, the first step was to calculate the mode of the red and blue fluxes that was used as a first estimate of the baseline fluxes.

The light curves were then subjected to a “filter” that selects light curves having one or more groups of points with fluxes sufficiently above the baseline flux, f_{base} . Such groups were initiated with any point i having a flux f_i greater than $f_{\text{base}} + 2.5\sigma_i$ where σ_i is the estimated uncertainty of f_i . The groups ended with the first subsequent sub-group of three points all with $f_i < f_{\text{base}} + 2\sigma_i$. The relative significance of the groups on a light curve was defined by

$$LP_N = N \log 2 - \sum_{i=1}^N \log \left[\operatorname{erfc} \left(\frac{f_i - f_{\text{base}}}{\sqrt{2}\sigma_i} \right) \right],$$

where N is the number of points in the group. For each red or blue light curve, groups having at least 5 points with $f_i > f_{\text{base}} + 2.5\sigma_i$ were then ordered by decreasing significance. A light curve was then retained for further analysis if one of the two most significant red groups had a temporal overlap of at least 20% with one of the two most significant blue groups.

Roughly 3% of the light curves pass this filter. The filter’s effective threshold is sufficiently low that, for clump stars, the filter passes essentially all microlensing events with apparent amplifications greater than 30% occurring during well-sampled parts of the observing period. Significant losses of efficiency occur due to bad weather, equipment failure and limited visibility of the Galactic Bulge at the beginning and end of each season.

Light curves passing the filter were then fit in each color with the microlensing light curve corresponding to uniform motion of an unblended point source and single lens. The total flux as a function of time is

$$f(t) = f_{\text{base}} \frac{u^2 + 2}{u \sqrt{u^2 + 4}} \quad (8)$$

where the impact parameter $u(t)$ is

$$u^2(t) = u_0^2 + \frac{(t - t_0)^2}{t_E^2}. \quad (9)$$

For each color, there are 4 fitted parameters: the baseline flux f_{base} , the time of maximum apparent amplification t_0 , the impact parameter at maximum amplification normalized to the Einstein ring radius $u_0 = u(t_0)$, and finally, the microlensing event duration, i.e. the Einstein ring radius crossing time $t_E = r_E/v_t$ for a transverse relative velocity v_t . The last two quantities depend on the Einstein radius, $r_E^2 = 4GMD_1(D_s - D_1)/c^2D_s$, where M is the mass of the lens, and D_1 and D_s are the distances to the lens and source, respectively.

While all transient flux variations can be fitted more or less successfully with the above expression, ideal microlensing events are characterized by achromaticity, i.e. the same u_0 , t_E and t_0 in all pass-bands. Because of the rarity of the

phenomenon, one generally also expects the events to be not repeated for a given star. A final important characteristic is that the detection efficiency corrected distribution of u_0 is flat. These characteristics guide the final selection of microlensing candidates. This selection is based on seven criteria, C1-C7, applied to the parameters of the microlensing fit performed on light curves passing the filter. The cuts we use lead to a detection efficiency that is relatively independent of u_0 so the flat distribution of u_0 is only moderately distorted. On the other hand, the cuts necessarily result in an efficiency that depends on t_E since very short events have a significant chance of falling between observations. The cuts are also sufficiently loose to maintain a good efficiency for finding non-conventional microlensing events, e.g. those due to binary lenses.

The first five criteria, C1-C5, are applied independently to the parameters of the fits for both bands and events are required to pass the criteria in both. C1 requires that the time of maximum apparent amplification be within the observing season so that the microlensing fit will yield reliable lensing parameters:

$$\text{C1 : } t_0 \in \text{observing season}$$

The beginning and end of the seven observing seasons were defined separately for each of the 66 fields by the first and last successful images for that field. For each field, only seasons with a mean sampling interval of less than 8.5 days are used. Sub-fields covered by CCD 2 were ignored for the first 4 seasons when the red CCD-2 was mostly out of order.

The second cut eliminates very long candidate events:

$$\text{C2 : } t_E < 400 \text{ d .}$$

A visual scan of events eliminated by this cut indicates that they are generally low amplitude events ($u_0 > 0.8$). No high amplitude microlensing events ($u_0 < 0.5$) were seen. Many of the $t_E > 400$ d events appear to be simple baseline shifts, with most occurring when the telescope optics were realigned at $t = JD - 2,450,000 = 983$. Most stars with such shifts are near very bright stars and it is probable that the shifts are due to slight changes in the wings of the PSF.

The third cut eliminates events due to known equipment problems. Most importantly, we eliminate long events occurring before $t = JD - 2,450,000 = 900$ by requiring

$$\text{C3 : } t_e < 100 \text{ d if } t_0 < 900 .$$

A visual scan of the ~ 5000 events eliminated with this cut indicates that almost all are due to the aforementioned baseline shifts at $t = 983$ which yielded events with $t_0 \sim 800$. We also eliminated 48 events on CCDs 6 and 7 between days 2323 and 2343 that were due to an electronics problem.

The next cut requires sufficient sampling during the event

$$\text{C4 : } \geq 4 \text{ points with } |t - t_0| < t_E ,$$

$$\text{and } \geq 8 \text{ points with } |t - t_0| < 2t_E .$$

This cut has the largest influence on the t_E dependence of the efficiency.

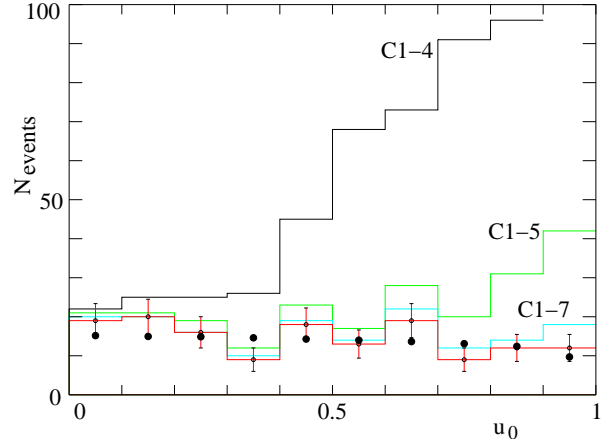


Fig. 6. The evolution of the u_0 distribution with the applied candidate selection criteria. The first histogram is for the 577 events with $u_0 < 1.0$ satisfying criteria C1, C2, C3 and C4. The second is for the 234 events that satisfy the five criteria C1-C5 and the third for the 165 events satisfying the seven criteria C1-C7. In the final histogram, 18 events have been eliminated whose light curves show additional variations outside the main variation or are clearly baseline shifts. The dots give the Monte-Carlo distribution for microlensing events satisfying all criteria.

Cut 5 is a very loose cut on the χ^2 of the microlensing fit calculated using only the points far from the time of maximum amplification, $|t - t_0| > 2t_E$:

$$\text{C5 : } \chi_{\text{base}}^2 / N_{\text{dof}} < 10 .$$

This cut eliminates most periodic and chaotic variable stars but retains single excursion events, even those that fit badly the simple light curve (8), e.g. events due to binary lenses.

Cuts 6 and 7 require reasonable agreement between the blue and red light curves:

$$\text{C6 : } \frac{t_0(\text{blue}) - t_0(\text{red})}{\langle t_E \rangle} < 0.4 ,$$

$$\text{C7 : } \frac{t_E(\text{blue}) - t_E(\text{red})}{\langle t_E \rangle} < 0.3 .$$

For the most part, these two cuts eliminate short time-scale excursions due to photometric problems on single exposures.

To understand the effect of each cut it is interesting to follow the evolution of the u_0 distribution as successive cuts are applied. The first distribution in Figure 6 is for the 577 events with $u_0 < 1.0$ that pass cuts C1, C2, C3 and C4. The distribution is dominated by events with $u_0 > 0.5$ corresponding to low amplitude variations. This is indicative of contamination by low amplitude variable stars. However, already with just these cuts, the distribution is flat for $u_0 < 0.4$ indicating that there is little background for high apparent amplification microlensing events.

The second distribution is for the 234 events that also satisfy C5. This eliminates most of the variable stars, and the u_0 distribution is now quite flat for $u_0 < 0.8$. Application of cuts C6 and C7 eliminate a few additional events, mostly near

event type	number	$\sum(t_E/\epsilon)/\text{total}$
simple	104	0.77
strong blends (B)	5	0.02
strong parallax (P)	4	0.11
binary non caustic (X)	2	0.02
caustic (C)	5	0.06
single excursion (?)	3	0.01
chaotic/periodic variable or baseline shift	6	-

Table 1. The tentative classifications of the 129 events satisfying cuts C1-C7 and $u_0 < 0.75$. The symbols in parentheses (B,P,X,C,?) show how these classifications are designated in Figure 8 and Table 3. The last column gives the relative weight of each classification if they were used in the calculation of the optical depth using the t_E from the simple-lens fit. (In reality, only 120 events are used, eliminating the 3 single excursion (?) events and 6 chaotic/periodic variables or baseline shifts.)

$u_0 \sim 1$, leaving 165 events with a distribution that is flat for $u_0 < 1.0$.

The 165 light curves were then visually examined. Most events fit well the simple microlensing light curve though a significant fraction show interesting effects. A summary of the scan conclusions is given in Table 1 for the 129 events with $u_0 < 0.75$ where there is generally little ambiguity about the nature of the events. Non-simple microlensing events include four strong parallax events, i.e. those with light curves strongly affected by the circular motion of the Earth (P). There are five binary lens events with visible caustic crossings (C). Five events show strong source blending (B) and are discussed in more detail in Section 6. Two events (X) show achromatic deviations from the simple lens curve that might be due either to non-uniform motion of the source in a binary system (i.e. a so-called xallarap event) or to a binary lens without caustic crossing. Six events show chaotic or periodic variations outside the primary variation and are therefore clearly not microlensing events. Finally three events marked (?) show single excursions that fit badly the simple lens curve but could conceivably be due to binary lenses.

The events with $u_0 > 0.75$ are visually not very striking, and a non-negligible number were eliminated by scanning. We therefore choose to eliminate these events so that for the remainder of this paper, we consider only the 120 events selected by C1-C7 and classified as microlensing events with $u_0 < 0.75$, i.e. maximum amplifications $A_{\max} > 1.6$. The characteristics of the 120 events are listed in Table 3. Figures 21, 22 and 23 show the light curves of three candidate events, the first with the most significant improvement in χ^2 over the constant-flux light curve, the second with the median improvement, and the third with the least significant improvement. All of the 120 light curves can be found on our web page, <http://eros.in2p3.fr>.

The u_0 distribution for the selected events is quite flat, as can be seen in Figure 6. It agrees with the expected distribution from the Monte-Carlo simulation. The fact that the observed

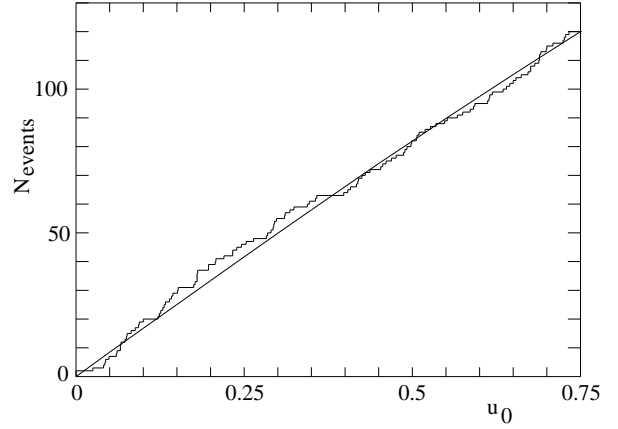


Fig. 7. The cumulative u_0 distribution for the 120 selected events. The smooth curve shows the efficiency-corrected flat u_0 distribution.

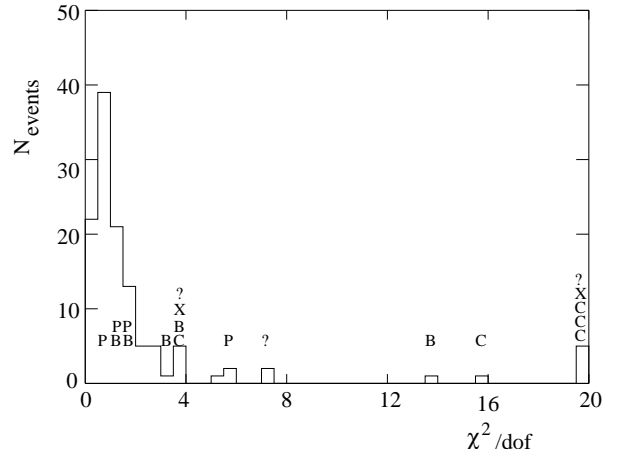


Fig. 8. The distribution of the reduced χ^2 calculated using points within the range $|t - t_0| < 2t_E$. The 120 accepted events plus the 3 (?) events appear in the plot. The letters show the positions of the 19 non-simple events as described in Table 1.

and expected distributions fall slightly near $u_0 = 1$ is due to the effect of the event filter that requires a sufficient number of points significantly above the baseline. Figure 7 shows the cumulative u_0 distribution for the 120 events and the efficiency-corrected curve for a flat u_0 distribution (with the observed distribution of t_E). The Kolmogorov-Smirnov test gives a CL of 83%. As discussed in Section 6, the sample may have a $\sim 10\%$ contamination at large u_0 by blended events due to the microlensing of faint background stars. Eliminating any randomly selected 10 events in the expected range $0.5 < u_0 < 0.75$ yields a CL of 34%, still quite acceptable.

The distribution of χ^2 per degree of freedom calculated for points in the range $|t - t_0| < 2t_E$ is shown in Figure 8. The simple events have a reasonable distribution with a mean value of 1.24, a quite satisfactory value considering the difficulty of estimating photometric uncertainties. The other categories of events have, naturally, larger values of reduced χ^2 , especially caustic events (C).

Figure 9 shows the scatter plot of $\log(t_E)$ vs. u_0 . The u_0 distribution is, as expected, not strongly dependent on t_E . Figure

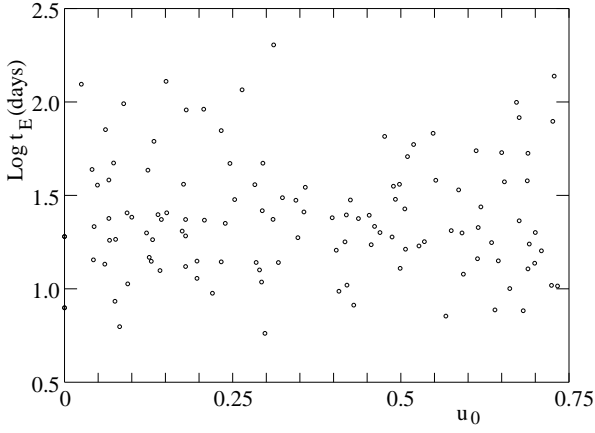


Fig. 9. The distribution of (u_0, t_E) for the 120 events passing all selection criteria with $u_0 < 0.75$.

10 shows the distribution of event magnitude and color relative to the center of the clump. The events show a distribution that is very similar to that of the ensemble of clump stars.

The events in the sample are generally well described by the light curve (8), as indicated by the reduced χ^2 distribution (Figure 8). Further indication that the events are indeed microlensing events comes from their achromaticity and time symmetry. Figure 11 shows that the events have equal u_0 and t_E in the blue and red as expected for microlensing events with negligible blending. Figure 12 shows that the events have equal rise and fall times. This test for time symmetry was performed by fitting the light curves with the form (8) with t_E in (9) modified by

$$t_E \rightarrow \Delta t = t_E \left[1 + \alpha \arctan\left(\frac{t - t_0}{t_E}\right) \right]. \quad (10)$$

The parameter α describes the asymmetry of the light curve with $\alpha = 0$ corresponding to a symmetric (microlensing) curve and $\alpha > 0$ ($\alpha < 0$) corresponding to rise times less than (greater than) the fall time. As an example, supernova light curves generally give $\alpha > 0.3$. The observed distribution (Figure 12) is symmetrically peaked at $\alpha = 0$ as expected for microlensing events.

5. Optical depth and t_E distribution

To determine the optical depth and the distribution of t_E , we must first evaluate the detection efficiency as a function of time scale t_E by using Monte-Carlo simulated light curves. We superimpose artificial microlensing events, with randomly generated parameters (impact parameter, date of maximum amplification and time scale), on a random sample of real light curves. These light curves are then subjected to the same microlensing search as the original light curves and we determine the fraction that are recovered by our detection algorithm. More precisely, the detection efficiency as a function of t_E is given by the ratio between two numbers:

- The number of events passing all selection criteria and with the reconstructed t_E within the considered t_E bin and with the reconstructed $u_0 < 0.75$.

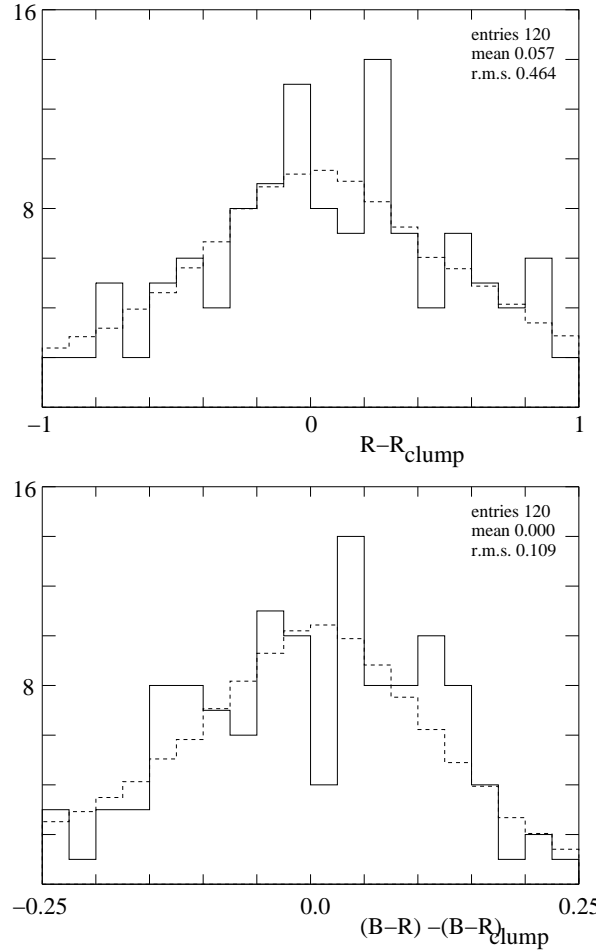


Fig. 10. The top panel shows the distribution of R_{eros} relative to the center of the clump, R_{clump} . The bottom panel shows the distribution of $(B - R)_{\text{eros}}$ relative to the center of the clump, $(B - R)_{\text{clump}}$. In both cases, the dashed histogram shows the distribution of random clump stars.

- The number of generated microlensing events with generated t_E within the considered t_E bin, with generated t_0 within the observing period for the field in question and with the generated $u_0 < 0.75$.

Figure 13 shows the efficiency as a function of t_E for a subsample of individual fields. The efficiency is field-independent at the 10% level. For $t_E > 100$ d criterion C3 causes a slight discontinuity in the efficiency for fields that were well observed during the first two seasons.

The microlensing optical depth is defined as the probability that a given star, at a given time t , is magnified by at least 1.34, i.e. with an impact parameter $u(t) < 1$. The optical depth is then given by

$$\tau = \frac{\pi}{2u_0(\text{max})} \frac{\sum_{i=1}^{N_{\text{ev}}} t_{E,i} / \epsilon(t_{E,i})}{\sum_{j=1}^{N_{\star}} T_j}, \quad (11)$$

where N_{\star} is the number of monitored stars, T_j is the observation period for star j , $t_{E,i}$ is the measured Einstein crossing time of the i th candidate and $\epsilon(t_{E,i})$ is the detection efficiency.

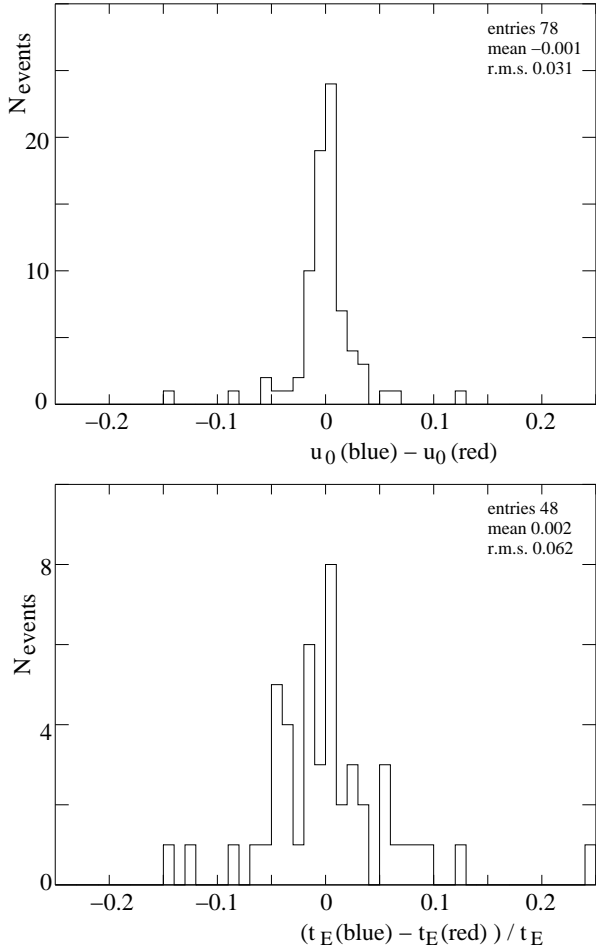


Fig. 11. Tests for achromaticity of the events. The top panel shows the difference between red and blue minimum impact parameters, u_0 , for the 78 events with at least three points in the range $t_0 - t_E/2 < t < t_0 + t_E/2$ for both red and blue curves, ensuring a precise measurement of the maximum amplification in both colors. The bottom panel shows the difference between red and blue t_E for the 48 events with at least three points in the range $t_0 - 3t_E/2 < t < t_0 - t_E/2$ and three points in the range $t_0 + t_E/2 < t < t_0 + 3t_E/2$ for both red and blue curves, ensuring a precise measurement of t_E in both colors.

For each event, the efficiency is taken from the corresponding subfield consisting of one CCD (Figure 13).

The denominator of (11) is $6.62 \times 10^9 \text{star} \cdot \text{days}$. Using the 120 events in Table 3, we find a calculated optical depth averaged over all fields which is

$$\tau = 1.68 \pm 0.23 \times 10^{-6}, \quad \langle |b| \rangle = 3.43^\circ. \quad (12)$$

The uncertainty is mostly statistical, estimated following the prescription of Han & Gould (1995b)

$$\sigma(\tau) = \tau \frac{\sqrt{\langle t_E^2 / \epsilon^2 \rangle}}{\langle t_E / \epsilon \rangle} \frac{1}{\sqrt{N_{ev}}} = 0.21 \times 10^{-6}. \quad (13)$$

To the statistical error we have added in quadrature a 5% systematic uncertainty due to blending effects, as discussed in

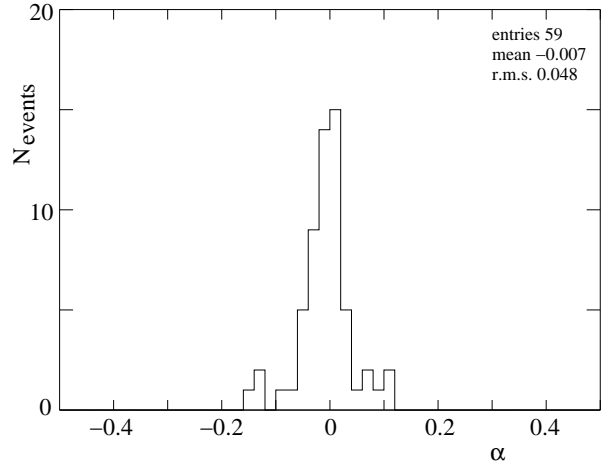


Fig. 12. Test for time symmetry of the events. The histogram is of the parameter α defined by (10) for events with t_0 at least 50 days away from both the beginning and the end of the observing season, ensuring a good measurement of α .

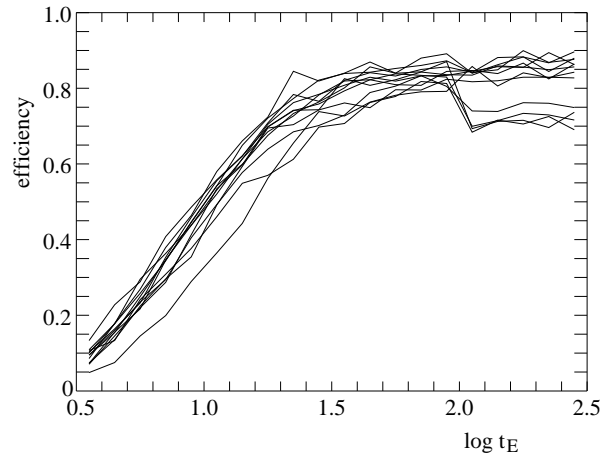


Fig. 13. Detection efficiency for individual fields as a function of the event time scale t_E (in days) for $u_0(\text{max}) = 0.75$. For the sake of clarity, only 12 of the 66 fields are shown. The discontinuity at $t_E = 100\text{d}$ is due to criterion C3 for fields that were observed during the first two seasons.

Section 6. The location and contribution of each of the 120 candidates to the measured optical depth is shown in Figure 14.

Because of the rapid variation of the optical depth across our fields, the above mean optical depth is of limited interest. Table 2 and Figure 15 shows the depth for various slices in Galactic latitude and longitude. The latitude gradient is clearly seen. Fitting the five points shown in Figure 15a, one finds

$$\tau / 10^{-6} = (1.62 \pm 0.23) \exp[-a(|b| - 3^\circ)], \quad (14)$$

with

$$a = (0.43 \pm 0.16) \text{deg}^{-1}. \quad (15)$$

At $b = -2.7^\circ$ this corresponds to an optical depth gradient of $(0.78 \pm 0.27) \times 10^{-6} \text{deg}^{-1}$, in agreement with the less precise values of MACHO (Popowski et al. 2005) $(1.06 \pm 0.71) \times 10^{-6} \text{deg}^{-1}$ and of OGLE-II (Sumi et al. 2006) $(0.78 \pm 0.84) \times$

range	$\langle b \rangle$	N_{stars}	N_{ev}	$\langle t_E \rangle$	$\sigma(t_E)$	$\langle t_E \rangle_{\text{cor}}$	$\tau/10^{-6}$
$1.40 < b < 7.00$	3.34	5569216	120	32.95	31.07	28.31 ± 2.84	1.68 ± 0.22
$1.40 < b < 2.00$	1.75	630884	25	29.17	21.85	24.88 ± 4.37	3.52 ± 1.00
$2.00 < b < 2.50$	2.26	829123	22	39.29	28.20	30.91 ± 6.01	2.38 ± 0.72
$2.50 < b < 3.00$	2.76	976707	24	22.87	15.49	20.89 ± 3.16	1.31 ± 0.38
$3.00 < b < 3.50$	3.23	931147	25	37.17	37.31	33.26 ± 7.46	2.21 ± 0.62
$3.50 < b < 7.00$	4.45	2194599	24	36.75	41.51	32.60 ± 8.47	0.92 ± 0.27
$-3.50 < b < -1.40$	2.69	1861880	54	35.68	30.22	31.33 ± 4.11	2.42 ± 0.47
$1.40 < b < 3.50$	2.50	1512735	42	27.27	23.42	23.08 ± 3.61	1.94 ± 0.42
$-6.00 < \ell < -3.00$	2.40	361293	10	46.02	28.13	39.43 ± 8.89	2.90 ± 1.30
$-3.00 < \ell < 0.00$	2.42	660722	20	29.79	23.56	25.65 ± 5.27	2.32 ± 0.73
$0.00 < \ell < 3.00$	2.22	981742	31	27.38	21.75	23.77 ± 3.91	2.20 ± 0.56
$3.00 < \ell < 6.00$	2.53	316650	8	25.93	11.89	23.88 ± 4.20	1.65 ± 0.83

Table 2. The measured optical depth for various slices in Galactic latitude b and Galactic longitude ℓ .

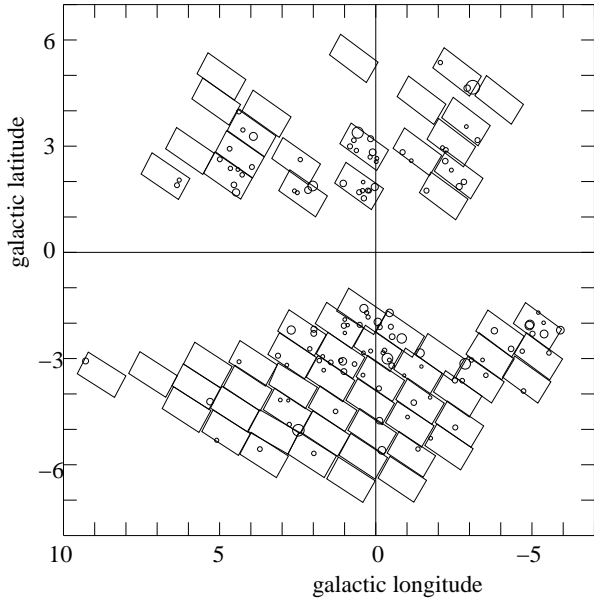


Fig. 14. The location of the 120 candidates used for the calculation of the optical depth. The area of each circle is proportional to the contribution of each candidate to the optical depth.

10^{-6}deg^{-1} . We see no significant difference between the northern and southern fields, as expected.

The dependence on Galactic longitude is expected to be much weaker. Additionally, nonuniform placement of the observing fields makes it easy to mask a longitudinal dependence by the stronger latitude dependence. Figure 15b shows the measured optical depth as a function of longitude for EROS-2 fields in the latitude range $1.4^\circ < |b| < 3.0^\circ$. Also shown are predictions for our fields of various models. No significant longitudinal dependence is seen.

Figure 16 shows the t_E distribution of the 120 events, both raw and efficiency corrected. The mean t_E (Table 2) is

$$\langle t_E \rangle = (28.3 \pm 2.8) \text{ d} . \quad (16)$$

We see no statistically significant latitude or longitude dependence of $\langle t_E \rangle$ (Table 2). The north-south difference,

$$\langle t_E \rangle_{b>0} - \langle t_E \rangle_{b<0} = (8.2 \pm 5.5) \text{ d} , \quad (17)$$

is not significant. Figure 17 shows the cumulative t_E distribution of the 120 events showing their contribution to the optical depth; 10% of the optical depth comes from the 24 events with $t_E < 13.6$ d and 10% from the 4 events with $t_E > 120$ d.

The 15% error in the optical depth (14) and 10% error in $\langle t_E \rangle$ (16) are mostly statistical, reflecting the number of events and the distribution of t_E . We believe that it is unlikely that any systematic errors are this large.

The most obvious systematic error would come from possible contamination of the event sample with events not due to microlensing. This is a serious problem for microlensing searches in the Magellanic Clouds. We note however that the Magellanic microlensing rate is at least a factor 10 lower than in the Galactic Bulge. Furthermore, the identified Magellanic background events should not be a problem here since they concern stars that are not in the clump region (blue bumpers, Be stars) or background supernovae that have light curves sufficiently different from microlensing light curves to be easily identified for the high signal-to-noise ratio events considered here. At any rate, there is no indication that our sample of 120 events is contaminated with events not due to microlensing. Among the indications for lack of significant contamination are

- The χ^2 distribution (Figure 8) indicates that the function (8) is a good description of the light curves.
- The u_0 distribution is nearly flat as expected (Figures 6 and 7).
- The events show no sign of chromaticity (Figure 11).

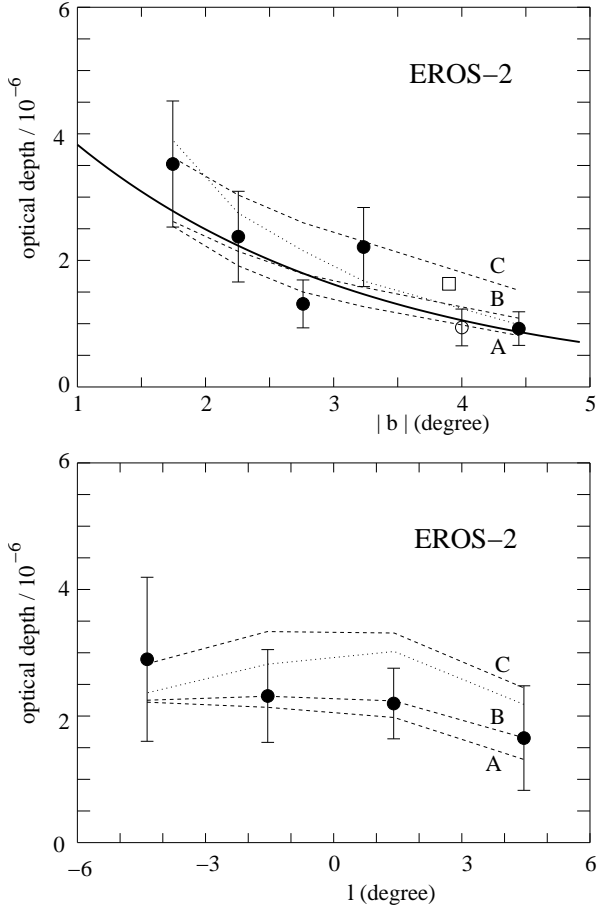


Fig. 15. The top panel shows the EROS-2 measured optical depth as a function of Galactic latitude. The bottom panel shows the optical depth as a function of Galactic longitude for the latitude range $1.4^\circ < |b| < 3.0^\circ$. The filled circles are from this work while the open circle in the upper panel is from the first EROS-2 analysis (Afonso et al. 2003b). In the upper panel, the solid line shows the fit (14). In both panels, the dotted lines show the prediction of the model of Bissantz & Gerhard (2002) and the dashed lines, A, B and C, show the predictions of three models used by Evans & Belokurov (2002) as described in Section 7. The open square in the upper panel is the prediction for the Baade Window by Han & Gould (2003).

- The light curves are symmetric about the time of maximum amplification (Figure 12).
- The optical depth has the expected dependence on the Galactic latitude (Figure 15). A background of variable stars might be expected to yield a measured optical depth that is latitude-independent.

A second systematic error could come from the contamination of the source sample by stars not in the Galactic Bulge. The number of source stars that are not in fact in the Galactic Bulge can be estimated from the general luminosity function and standard Galactic models. Generally, one finds that less than 1% of the stars in the clump box (Figure 3) could be foreground main sequence stars. For negative latitudes, a contribution at the percent level can also be expected from bright giants in

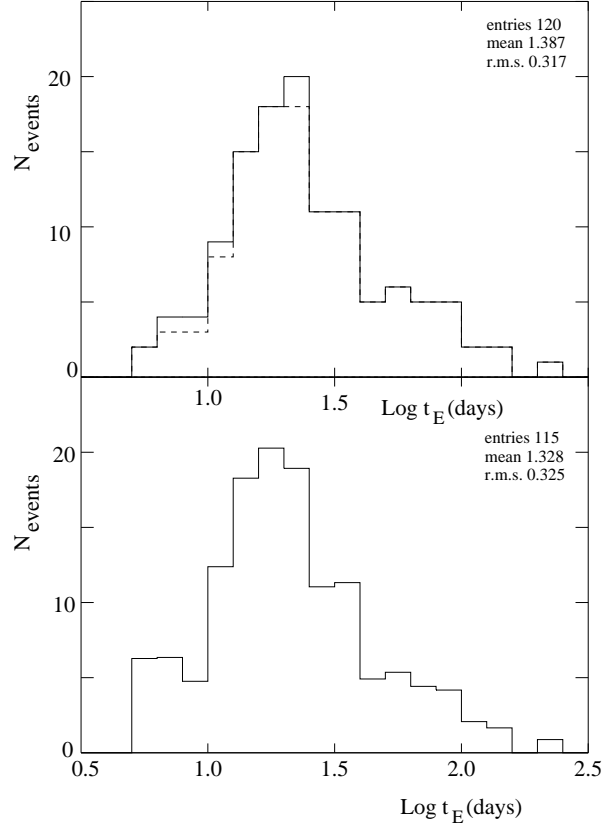


Fig. 16. The distribution of Einstein radius crossing times, t_E . The top panel shows the raw distribution for the 120 events with $u_0 < 0.75$ with the dashed line corresponding to the 115 events that show no strong blending. The bottom panel shows the distribution corrected for the t_E dependence of the detection efficiency.

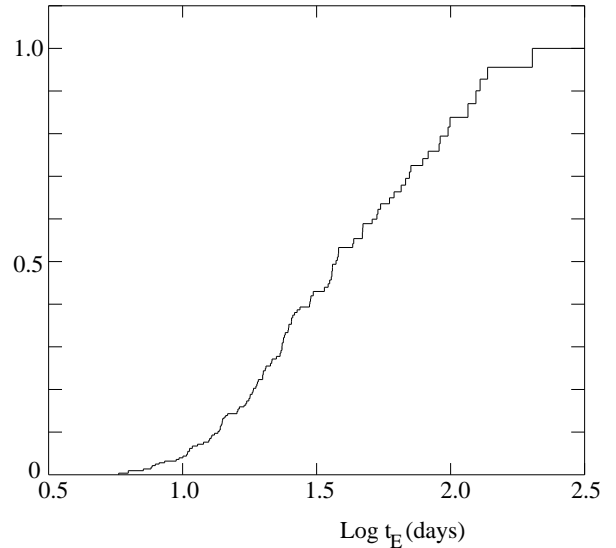


Fig. 17. The normalized cumulative distribution of the contribution of the 120 candidates to the observed optical depth as a function of t_E . 10% of the optical depth comes from the 24 events with $t_E < 13.6$ d and 10% from the 4 events with $t_E > 120$ d.

the Sagittarius dwarf galaxy where stars are ~ 2.3 mag dimmer than low-latitude stars in the Galactic Bulge (Alard 1996).

A third effect comes from the preferential selection of source stars on the near side of the Bulge because the magnitude cut on source stars (Figure 3) favors stars on the near side. Compared to a star at the Galactic center, stars on the near (far) side of the bulge are shifted upward (downward) in the color-magnitude diagram. Faint stars on the near side are moved into the accepted magnitude range while bright stars move out. Since there are more dim stars than bright stars, there is a net gain of stars on the near side. The opposite effect occurs on the far side where there is a net loss of stars. We used a Monte-Carlo calculation to estimate the mean position of our source stars and found that it is shifted towards us from the Galactic center by about 5% of the r.m.s. Bulge light of sight thickness. Since stars on the near side have a lower than average optical depth for bulge-bulge lensing, we can expect that the optical depth is underestimated by of order 5%. This factor is not negligible compared to the statistical errors and any precise comparison with Galactic models will require that models properly weight source stars by their position in the Bulge.

A fourth effect could be the misclassification of non-standard microlensing events (e.g. caustic events) as variable stars. Our detection criteria are sufficiently liberal that several clear binary events were found, making up about 8% of the optical depth (Table 1). The ambiguous single excursion events would be only about 1% of the optical depth if they were included in the calculation. It therefore seems unlikely that there is a loss of events at the 10% level.

A fifth systematic error could come from the use of the t_E fitted with (8) for events due to non-standard lenses. The problem is minor for parallax events for which the modifications of (8) are relatively small and the use of the fitted t_E makes little difference. On the other hand, caustic events have light curves that resemble (8) only in the wings and the fitted t_E can be far from its true value, though for the caustic events in this study, the differences are only of order 10%. At any rate, the number of events of this category is small, so we can expect that the modification of the calculated optical depth should be much less than 10%. This was the conclusion of the detailed study of Glicenstein (2003).

The sixth systematic effect is that due to blending, the subject of the next section.

6. Effect of blending on the measured optical depth

Stellar blending complicates the interpretation of microlensing events in crowded fields. It is helpful to divide blending into two effects:

- Effect I: The photometry of bright (clump giant) stars is affected by the background of faint stars that are randomly placed with respect to the bright star. In the photometry, the sky background is assumed to be a smooth function so if the number of faint stars inside the seeing disk of the bright star is greater than the average number, the baseline flux of the bright star will be overestimated and the amplification

due to microlensing underestimated. The opposite will occur if the number of faint stars is smaller than average. We can therefore expect that on average amplifications are correctly estimated. However, as emphasized in the previous section, the magnitude cut (Figure 3) used to select source stars favors stars whose baseline fluxes are overestimated. We therefore expect a slight underestimation of the amplification.

- Effect II: The microlensing of a faint star within the seeing disk of a bright star will cause the reconstructed flux of the bright star to vary in time, yielding an apparent microlensing of the bright star.

By itself, effect II will clearly cause one to overestimate the optical depth if (11) is used since some of the events will not be due to the N_{star} clump giants. On the other hand, we expect that effect I goes in the opposite direction since amplifications of clump giants are on average underestimated. Because of this, the reconstructed t_E found using (8) are systematically underestimated while the reconstructed u_0 are overestimated. In the formula (11) for the optical depth, the terms in the sum are therefore underestimated on average. Furthermore, fewer events are included in the sum because the overestimation of u_0 causes some events to migrate beyond $u_0(\text{max})$. Effect I therefore, by itself, causes the optical depth to be underestimated.

To estimate the importance of blending we have performed two types of tests with artificial stars placed on CCD images. The first type uses totally synthetic images in which all stars are artificial. This was used to quantify the sum of effects I and II. The second type uses real EROS-2 images in which artificial clump giants are added at random places on the images. This was used to quantify effect I.

The production and analysis of the totally synthetic images were described in the first EROS-2 Galactic Bulge article (Afonso et al. 2003b). Series of CCD images were produced by placing on them stars taken randomly from the luminosity distribution observed for the Baade window in HST deep images (Holtzman et al. 1998). The HST luminosity distribution extends to 9 magnitudes fainter than clump giants and therefore allowed us to simulate the bright stars used in the EROS-2 analysis as well as the fluctuating background of faint stars. Microlensing events were assigned to a subsample of stars and the resulting flux change was taken into account when placing charge on the CCD. The sequence of CCD images were then reconstructed in the same way as normal EROS-2 images and events were searched for.

The results of this study indicated that reconstructed amplifications are indeed underestimated for clump giant stars leading to an underestimation of the optical depth (effect I) but that this is compensated to a precision of about 5% by events due to background stars (effect II). For the analysis of Afonso et al. (2003b), about 18% of the recovered optical depth was due to these faint stars compensating for the 15% underestimation for those events due to bright stars. For the analysis presented here, the effects are smaller because brighter stars are used and the amplification threshold is higher (1.6 instead of 1.34). We now find that only about 6% of the recovered optical depth is expected to be due to faint background stars.

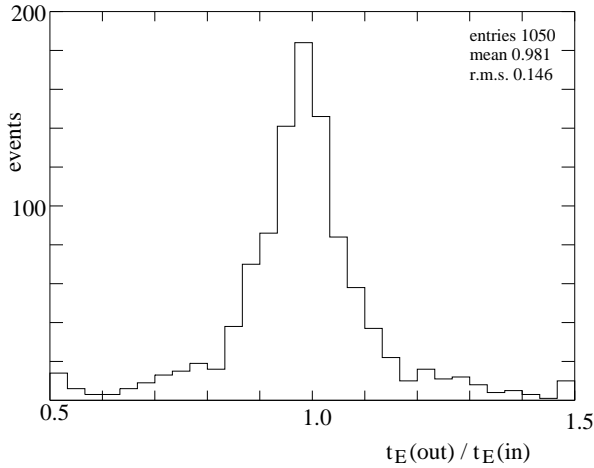


Fig. 18. The ratio of recovered and generated values of t_E for artificial clump giants placed on EROS-2 field 610.

Our second test used partially synthetic images on which we placed artificial clump giants on the real EROS-2 CCD images. As in the first test, microlensing events were simulated by giving the artificial giants time-dependent fluxes. These so-called spiked images were then photometered by the normal procedure and the events recovered and fitted with the microlensing light curve.

Figure 18 shows the comparison between recovered and simulated t_E . This parameter is correctly estimated on average with 85% of events yielding a t_E within 20% of the generated t_E . The 15% of events in the wings are due to stars whose baseline flux was strongly overestimated or underestimated because of blending. The nearly symmetric shape of the distribution in Figure 18 means that a bias in the reconstruction of t_E results mostly from the fact that the magnitude cuts favor stars whose flux was overestimated. The distribution in Figure 18 and the associated correlation with reconstructed baseline flux was thus combined with the observed magnitude distribution to make a Monte-Carlo estimate of the optical depth bias. The results confirm that effect II causes $\sim 5\%$ underestimation of the optical depth.

Since these images only give information on effect II, we supplement it with a simple numerical calculation to estimate the contribution of faint stars in the seeing disk. A microlensed faint star superimposed on a bright star yields a light curve given by

$$F(t) = F_s \left[(1-f) + f \frac{u^2 + 2}{u \sqrt{u^2 + 4}} \right], \quad (18)$$

where f is the ratio between the faint star's baseline flux and the total reconstructed baseline flux. For $f \ll 1$, the reconstructed amplification is much less than the real amplification yielding reconstructed u_0 and t_E respectively much greater than and much less than the real u_0 and t_E . In practice, this means that stars more than 4 magnitudes fainter than clump giants yield no observable events because their reconstructed t_E are less than 5 d. The HST luminosity function gives on average about 3 stars within 2 arcsec of a clump giant and within 4 magnitudes of the clump magnitude. Integrating the HST function,

we can expect that about 10% of clump giant events will be due to faint background stars. Since the events are much shorter than real clump giant events, they contribute only about 4% to the measured optical depth, not far from the above estimates.

Because of the approximate compensation, we make no blending correction to the optical depth. Instead, because of the difficulty in estimating the effect precisely, we choose to include a 5% uncertainty in the optical depth, i.e. an uncertainty equal to the estimated size of each of the compensating effects. This uncertainty is, at any rate, less than the statistical uncertainty of the present measurements. Future high statistics measurements of the optical depth will certainly have to be much more careful about blending, especially if faint source stars are used.

Some strongly blended events can be found by fitting light curves to a microlensing curve (18). Since all events are blended to some extent, the number of detected blends is a sensitive function of the photometric precision. Five EROS-2 events showed a significant improvement for this curve over that with the simple curve (8). The events are characterized by excess amplification in their wings due to the fact that the real t_E is greater than the t_E fitted with (8).

The absence of strong blending in most events is seen in Figure 19a showing $t_E(\text{blend})$ vs. $t_E(\text{no-blend})$. While the cloud of points is very wide because of the degeneracies in the fit, for the most part there is no systematic difference between the two t_E , whereas $t_E(\text{blend}) > t_E(\text{no-blend})$ for truly blended events. This is confirmed in Figure 19b, which shows the logarithm of the ratio of the two t_E 's both for the observed events and for the simulated clump giants. The observed distribution is very similar to the Monte-Carlo distribution.

The absence of strong blending for our events is not inconsistent with the results of the OGLE-II group who observed a large number of strongly blended events on clump giants. Most of the OGLE-II blended events are very low amplification events, ($u_0(\text{no-blend}) > 1$) with only 4 of their 26 events with $u_0(\text{no-blend}) < 0.75$ being characterized as blends. This proportion of blends is somewhat higher than our estimates, a fact that may be due to their superior photometric precision. At any rate, the number is sufficiently small to be of minor importance for optical depth determinations with $u_0 < 0.75$.

7. Discussion and Conclusions

The EROS-2 optical depth measurement presented here is in remarkably good agreement with the other clump-giant measurements shown in Figure 20, i.e. those of the MACHO group (Popowski et al. 2005) and OGLE-II group (Sumi et al. 2006). Only the original low statistics MACHO measurement (Alcock et al. 1997) is a bit too far from our fitted optical depth (14).

Figure 15 shows that our optical depth measurements are in reasonable agreement with some recent calculations based on models of the Galactic Bar and Disk. The dotted line in Figure 15 is the prediction of the non-parametric model of Bissantz & Gerhard (2002). The strong latitude dependence is correctly predicted as is the nearly flat longitude dependence. The three dashed lines correspond to calculations of

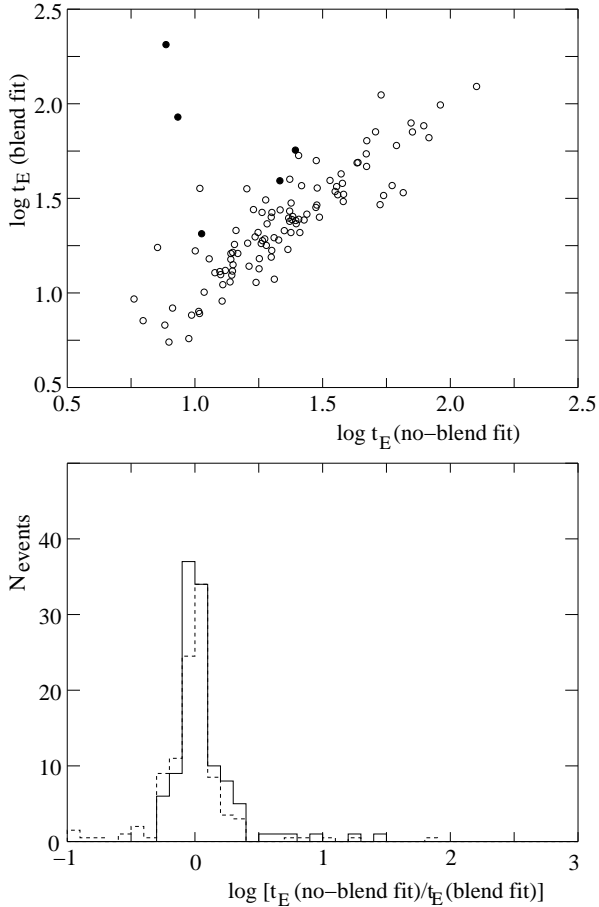


Fig. 19. The fitted t_E assuming blending (equation 18), vs. the fitted value assuming no blending (equation 8). The filled circles correspond to the five events showing strong blending. The bottom panel shows the logarithm of the ratio of the two t_E for simulated events (solid line) and observed events (dashed line).

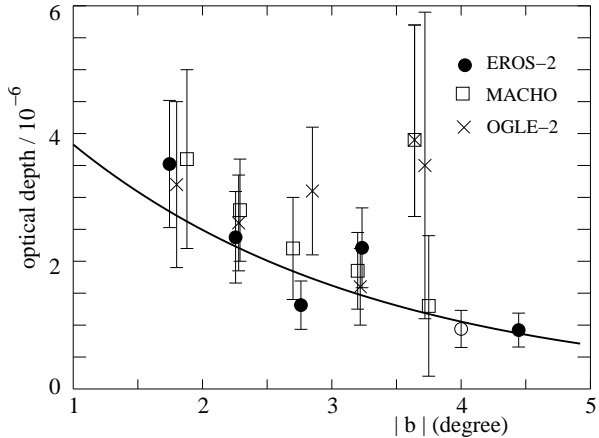


Fig. 20. Optical depth as a function of Galactic latitude. The filled circles are this work while the open circle is the first EROS-2 analysis (Afonso et al. 2003b). The solid line shows the fit (14). The measurements of the MACHO group are the open squares (Popowski et al. 2005) and the crossed square of the early analysis of Alcock et al. (1997). The crosses are from the OGLE-II group (Sumi et al. 2006).

Evans & Belokurov (2002) based on the three models of the inner Galaxy. Curve A is based on the model of Binney et al. (1997), curve B on the model of Dwek et al. (1995), and curve C on the model of Freudenreich (1998). (For these three models, we show the predictions without corrections due to spiral structure; these would give at most a 20% increase to the calculated optical depth.) All three models have a common total mass of $1.5 \times 10^{10} M_\odot$ within 2.5 kpc of the Galactic Center. The data in Figure 15 indicate that the “swollen bar” model of Freudenreich (1998) is not favored by the data, unless the assumed mass is reduced by $\sim 30\%$.

Finally, Figure 15 shows the Baade window prediction of Han & Gould (2003). The calculated optical depth is within one standard deviation of the curve given by (14).

We make no attempt here to separate the Disk (2) and Bulge (3) contributions so our conclusion is simply that the model of Bissantz & Gerhard (2002) or models A and B of Evans & Belokurov (2002) give a good estimate of the total optical depth (1). We note that these models place the bulk of the mass in normal stars and gas so the agreement with our measurements indicate that there is no need for additional mass in a non-lensing form. In models with cold dark matter, the dark component may make a significant contribution to the mass in the inner parts of the Milky Way. For example, in the models of Klypin, Zhao & Somerville (2002), the cold dark matter contribution to the rotation curve at 1 kpc from the Galactic Center is between 30% and 50%. Such a contribution would, by itself, lower the optical depth by roughly the same factor. Our optical depth measurement, with its 15% uncertainty, therefore provides a useful constraint on such models.

Galactic models generally suppose a smooth distribution of lenses and therefore predict a smooth longitude and latitude dependence of the optical depth. The MACHO group (Popowski et al. 2005) observed 9 events near ($\ell = 2.9^\circ$, $b = -2.9^\circ$) (their field 104), yielding an optical depth about 2 standard deviations above the expectation based on their other fields. As seen in Figure 14, we do not see an excess in this direction. Of their 9 events, 4 events occurred after the beginning of EROS-2. Of these 4 events, two are not in an Eros field and two are in our field 611. Both of these events were found (in Table 3, MACHO events 104.20515.498 and 104.20640.8423). No other EROS events were found in this region in the three bulge seasons after the shutdown of MACHO. The fact that EROS-2 saw only two events for a solid angle and time period equivalent to that in which MACHO found 9 events suggests that the MACHO excess is a statistical fluctuation.

While our optical depth measurement is in good agreement with other measurements and with Galactic models, agreement on the t_E distribution is less satisfactory. Our value of $\langle t_E \rangle$ is in excellent agreement with the value, (28.1 ± 4.3) d, found by OGLE-II (Sumi et al. 2006). The EROS-2 and OGLE-II values are, however, significantly higher than that calculated using the 62 MACHO events (Table 3 of (Popowski et al. 2005)): $\langle t_E \rangle = (21.6 \pm 3)$ d. The discrepancy lies entirely in the large number of MACHO events with $t_E < 10$ d. The number of MACHO events with ($t_E < 5$, $5 < t_E < 10$, $t_E > 10$ d) is (6, 14, 42) whereas the corresponding numbers for EROS-2 are (0, 10, 110). Part of the differences in event numbers is due to the fact the the MACHO

efficiency is relatively greater than the EROS-2 efficiency for $t_E < 10$ d. Using the 14 MACHO events with $5 \text{ d} < t_E < 10$ d and the relative efficiencies of the two experiments, we estimate that EROS-2 should see 24 ± 7 events in this range compared to the 10 that are seen. The very low EROS-2 efficiency for $t_E < 5$ d makes it unsurprising that we found no events in this range.

Whatever the source of the discrepancy, these short events have relatively little effect on the measured optical depths. The events with $t_E < 10$ d constitute only about 12% of the MACHO optical depth and only 4% of the EROS-2 optical depth.

The Galactic models are capable of reproducing the t_E distribution by adopting an appropriate stellar mass function. The model of Wood and Mao (2005) is in good agreement with our distribution and with that of OGLE-II, both with $\langle t_E \rangle \sim 28$ d. The model of Bissantz et al. (2004) is in good agreement with the distribution reported by MACHO with $\langle t_E \rangle \sim 21$ d. According to Wood and Mao (2005), the different $\langle t_E \rangle$ predictions of the two models is mostly due to different adopted mass functions leading to a mean lensing mass of $0.35 M_\odot$ for Wood and Mao (2005) and $0.11 M_\odot$ for Bissantz et al. (2004). Kinematical differences between the two models may also have a non-negligible effect.

The present comparison with models is still primarily limited by the low number of observed events. Since the EROS-2 survey uses most of the fields in the Bulge region that are easily observed in optical bands, a large increase in the number of monitored clump giants would require infrared observations of highly obscured regions near the Galactic Center (Gould 1995). Of course the number of events can also be increased by using dim stars but, in this case, reliable results would require a good understanding of blending.

Acknowledgements. We thank V. Belokurov and N.W. Evans for providing their microlensing maps in computer-readable form and O. Gerhard for interesting discussions. We are grateful to the technical staff of ESO, La Silla for the support given to the EROS-2 project. We thank J-F. Lecoq and A. Gomes for the assistance with the on-line computing and the staff of the CC-IN2P3, especially the team in charge of the HPSS storage system, for their help with the data management. AG was supported by grant AST-0452758 from the NSF and JA by the Danish Natural Science Research Council.

References

- Afonso, C., Albert, J. N., Andersen, J., et al. (EROS-2 coll.) 2003a, *A&A*, 400, 951
- Afonso, Albert, J. N., Alard, C. C., et al. (EROS-2 coll.) 2003b, *A&A*, 404, 145
- Alard, C. 1996, *ApJ*, 458, L17
- Alcock, C., Allsman R. A., Alves D. R., et al. (MACHO coll.) 1997, *ApJ*, 479, 119
- Alcock, C., Allsman R. A., Alves D. R., et al. (MACHO coll.) 2000a, *ApJ*, 541, 734
- Alcock, C., Allsman, R. A., Alves, D. R., et al. (MACHO coll.) 2000b, *ApJ*, 542, 281
- Ansari, R. (EROS-2 coll.) 1996, *Vistas in Astronomy*, 40, 519
- Bauer, F. et al. (EROS-2 coll.) 1997, Proceeding of the “Optical Detectors for Astronomy” workshop, ESO
- Benjamin, R.A., Churchwell, E., Babler, B. L., et al. 2005, *ApJ*, 630, L149
- Binney J., Gerhard, O. & Spergel D. 1997, *MNRAS*, 388, 365
- Binney, J., Bissantz, N. & Gerhard, O. 2000, *ApJ*, 537, L99
- Bissantz, N. and Gerhard, O. 2002, *MNRAS*, 330, 591
- Bissantz, N., Debattista, V & Gerhard, O. 2004, *ApJ*, 601, L155
- Calchi Novati, S., Paulin-Henriksson, S., An, J., et al. 2005, *A&A*, 443, 911
- de Jong, J. T. A., Widrow, L.M., Cseresnjcs, P., et al. 2005, *A&A*, 446, 855
- Derue F., Afonso C., Alard C., et al. (EROS-2 coll.) 2001, *A&A*, 373, 126
- Dwek E., Arendt, R. G., Hauser M. G., et al. 1995, *ApJ*, 445, 716
- Evans, N.W. & Belokurov, V. 2002, *ApJ*, 567, L119
- Freudenreich, H.T. 1998, *ApJ*, 492, 495
- Glicenstein, J.F. 2003, *ApJ*, 584, 278
- Gould, A. 1995, *ApJ*, 446, L71
- Griest, K. 1991, *ApJ*, 366, 412
- Hamadache, C. 2004, Thesis Université de Strasbourg, <http://tel.ccsd.cnrs.fr/>
- Han C. & Gould A. 1995b, *ApJ*, 449, 521
- Han, C. and Gould, A. 2003, *ApJ*, 592, 172
- Holtzman, J. A., Watson, A. M., Baum, W. A., et al. 1998, *AJ*, 115, 1946
- Joshi, Y.C., Pandey, A.K., Narasimha, D. & Sagar, R. 2005, *A&A*, 433, 787
- Kiraga M. & Paczyński B. 1994, *ApJ*, 430, L101
- Klypin, A., Zhao H. & Somerville, R. 2002, *ApJ*, 573, 597
- Le Guillou, L. 2004, Thesis Université de Paris VI, <http://tel.ccsd.cnrs.fr/>
- Paczynski, B. 1986, *ApJ*, 304, 1
- Paczynski B. 1991, *ApJ*, 371, L63
- Popowski P., Cook K. H., Drake A. J., et al. (MACHO coll.) 2000, In Menzies J.W., Sackett P.D. eds, Proc. Microlensing 2000, ASP Conference Series (astro-ph/005466)
- Popowski, P., Griest, K., Thomas, C. L., et al. 2005, *ApJ*, 631, 879
- Riffeser, A., Fliri, J., Bender, R., et al. 2003, *ApJ*, 599, L17
- Stanek, K.Z., Mateo, M., Udalski, A., et al. 1994, *ApJ*, 429, L73
- Sumi, T., Abe, F., Bond, I. A., et al. (MOA coll.) 2003, *ApJ*, 591, 204
- Sumi, T., Wozniak, P. R., Udalski, A., et al. (OGLE coll.) 2006, *ApJ*, 636, 240.
- Tisserand, P., et al. 2006, astro-ph/0607207, submitted to *A&A*; Tisserand, P. 2004, Thesis Université de Nice, <http://tel.ccsd.cnrs.fr/>
- Udalski A., Szymanski M., Kaluzny J., et al. (OGLE coll.) 1994a, *ApJ*, 426, L69
- Udalski A., Szymanski M., Stanek K. Z., et al. (OGLE coll.) 1994b, *Act. Astr.*, 44, 165
- Udalski A., Zebrun K., Szymanski M., et al. (OGLE coll.) 2000, *Act. Astr.*, 50, 1

- Udalski, A., Szymanski, M., Kubiak, M., et al.(OGLE coll.)
2002, Act. Astr., 52, 217
- Uglesich, R.R., Crots, A. P. S., Baltz, E.A., et al. 2004, ApJ,
612, 877
- Wood, A. and Mao, S. 2005, MNRAS, 362, 945
- Woźniak P. R., Udalski A., Szymanski M. et al. (OGLE coll.)
2001, Act. Astr., 51, 175

event	r.a	dec.	b	l	t_E	u_0	t_0	ϵ	note
607-1-4- 11480	270.2603	-29.0032	-2.942	1.698	12.780	0.689	1274.70	0.576	SC30-57488
607-3-3- 9841	270.2787	-29.3148	-3.110	1.441	17.354	0.691	716.60	0.577	M-113.19192.365
607-5-1- 14742	270.0417	-29.5630	-3.053	1.121	18.181	0.067	2113.40	0.713	
607-5-1- 29607	270.0288	-29.6350	-3.079	1.054	61.540	0.133	636.60	0.823	M-118.18797.1397
607-5-4- 20285	270.2924	-29.8155	-3.367	1.020	36.233	0.498	1315.50	0.810	M-118.19184.939
607-6-3- 29248	269.8908	-30.0002	-3.156	0.680	15.967	0.709	2137.00	0.560	
610-0-1- 17627	270.4365	-28.9678	-3.059	1.809	18.775	0.347	1775.80	0.671	SC30-636963
610-2-3- 4703	270.6194	-29.2331	-3.328	1.666	10.458	0.420	1988.40	0.497	
611-1-4- 24874	271.0400	-27.7431	-2.920	3.132	27.429	0.619	683.50	0.798	M-104.20515.498
611-3-4- 18476	271.1397	-28.1256	-3.184	2.849	13.708	0.699	998.40	0.706	M-104.20640.8423
612-7-4- 8538	271.8072	-32.0593	-5.593	-0.195	70.213	0.233	1019.10	0.867	
613-5-1- 23714	271.5512	-30.1737	-4.493	1.288	20.356	0.175	2144.10	0.722	
615-1-2- 22556	271.8863	-26.7402	-3.090	4.378	14.728	0.126	1599.30	0.650	
619-0-4- 7664	272.2137	-28.4529	-4.170	3.057	9.705	0.408	523.40	0.474	M-110.22455.842
619-5-4- 19755	272.7316	-29.0649	-4.862	2.769	16.290	0.507	1732.70	0.608	
619-7-4- 14204	272.7335	-29.4067	-5.026	2.478	116.099	0.264	1254.70	0.677	P
624-4-3- 3703	273.1066	-30.1842	-5.679	1.984	17.672	0.635	1414.90	0.588	
627-7-2- 14994	273.4693	-26.4997	-4.217	5.306	43.505	0.041	1958.20	0.692	
2-0-1- 13467	267.8171	-30.2087	-1.710	-0.441	59.171	0.519	2383.30	0.793	
2-0-4- 18520	268.1808	-30.4511	-2.103	-0.482	22.388	0.239	1707.10	0.682	
2-1-1- 5329	268.3954	-30.1464	-2.109	-0.125	26.760	0.506	2122.60	0.783	
2-3-3- 30438	268.4314	-30.6361	-2.383	-0.524	38.098	0.552	996.30	0.908	
2-5-1- 20157	268.2981	-30.9266	-2.432	-0.831	97.853	0.088	1726.80	0.863	C
3-4-3- 2992	268.1774	-29.4347	-1.585	0.381	65.395	0.476	2100.30	0.782	
3-4-3- 27217	268.2445	-29.5728	-1.705	0.294	14.034	0.129	1685.60	0.582	SC37-645044
3-5-2- 20099	268.3380	-29.6770	-1.828	0.248	14.104	0.645	1759.70	0.554	SC3-371229
3-5-3- 26926	268.6611	-29.5536	-2.008	0.501	23.762	0.437	1257.30	0.706	SC4-522952
3-6-4- 15890	268.2890	-30.0199	-1.965	-0.066	38.201	0.066	955.90	0.489	SC3-91382
4-3-2- 5389	269.2294	-30.2536	-2.786	0.164	16.954	0.527	1283.20	0.822	
4-3-3- 2508	269.4168	-30.0798	-2.839	0.397	13.941	0.233	1411.40	0.753	
4-4-4- 9143	268.9565	-30.6300	-2.770	-0.280	21.513	0.044	1719.10	0.797	B
4-5-2- 8464	269.0497	-30.6251	-2.837	-0.233	17.209	0.456	1985.60	0.744	
4-7-1- 7864	269.1321	-30.8306	-3.002	-0.370	137.482	0.728	2086.20	0.930	P
4-7-1- 20818	269.1327	-30.9075	-3.041	-0.435	14.483	0.614	2180.60	0.707	
4-7-2- 19218	269.2468	-31.0564	-3.200	-0.509	37.820	0.688	1833.10	0.912	SC22-414328
5-4-1- 8951	268.8382	-29.0702	-1.897	0.993	10.424	0.724	1093.70	0.537	
5-4-3- 22912	269.0256	-29.1386	-2.073	1.020	30.119	0.492	2063.00	0.825	
5-4-4- 11338	268.9376	-29.2330	-2.055	0.900	7.704	0.640	1271.10	0.411	B
5-5-2- 19037	269.2080	-29.2700	-2.277	0.992	7.912	0.000	1651.60	0.411	
6-1-3- 21678	270.0438	-30.3994	-3.468	0.411	13.550	0.060	1763.90	0.625	C
6-5-3- 18380	270.1206	-31.0448	-3.844	-0.102	23.286	0.208	2077.50	0.688	
8-3-1- 1345	270.1013	-27.7379	-2.195	2.709	78.728	0.726	1714.00	0.907	
8-4-2- 21125	269.7872	-28.4151	-2.290	1.986	34.932	0.358	948.70	0.801	X M-401.48408.649
8-4-2- 21623	269.6680	-28.3593	-2.171	1.979	43.148	0.124	2129.90	0.887	
8-7-3- 16227	270.2820	-28.5282	-2.724	2.114	19.994	0.469	1301.90	0.803	SC30-165305
9-7-4- 7143	271.0161	-31.5437	-4.755	-0.118	50.982	0.510	1450.80	0.914	
30-2-3- 19447	273.9211	-28.5940	-5.557	3.712	23.998	0.398	1698.10	0.758	
31-3-3- 35856	274.4120	-27.2411	-5.308	5.095	13.824	0.318	1628.90	0.503	
61-0-3- 8256	274.4475	-22.4102	-3.067	9.292	37.373	0.654	1743.70	0.781	
70-3-1- 18517	265.4297	-34.2263	-2.068	-4.914	90.589	0.181	1707.40	0.964	C
70-3-1- 18797	265.3838	-34.2285	-2.036	-4.936	91.418	0.207	2400.50	0.961	
70-3-4- 28566	265.5989	-34.4414	-2.300	-5.016	29.865	0.425	1602.40	0.871	
70-4-1- 17316	265.0553	-34.5743	-1.989	-5.374	7.140	0.567	1428.90	0.330	
70-5-2- 24247	265.3672	-34.7616	-2.306	-5.388	71.090	0.061	1842.60	0.890	
70-6-2- 31993	264.9205	-35.1415	-2.197	-5.908	46.872	0.246	1456.10	0.587	

71-3-1- 21364	266.2818	-33.3554	-2.214	-3.797	47.100	0.073	892.10	0.911	
71-7-1- 28518	266.4633	-34.0936	-2.727	-4.332	36.263	0.177	2024.70	0.906	C
72-1-1- 22000	266.3057	-34.4337	-2.792	-4.688	18.317	0.131	2343.10	0.722	
72-4-2- 12551	265.8097	-35.1914	-2.841	-5.544	21.568	0.461	1442.30	0.804	
73-3-4- 7001	267.3455	-33.4813	-3.040	-3.418	14.286	0.043	896.30	0.739	
74-5-3- 16791	267.4200	-35.0934	-3.917	-4.730	23.496	0.180	2177.00	0.793	
76-1-3- 12658	268.3605	-31.6522	-2.845	-1.417	82.468	0.676	1046.30	0.900	
77-0-1- 20761	267.5647	-33.1794	-3.042	-3.065	18.932	0.487	928.60	0.711	
77-0-3- 7242	267.7949	-33.0623	-3.149	-2.862	128.844	0.151	1628.20	0.883	P
77-1-4- 10694	268.3326	-33.2374	-3.625	-2.765	24.832	0.419	2005.60	0.853	
77-4-1- 13517	267.7165	-33.8108	-3.473	-3.525	23.493	0.144	1426.00	0.856	
78-4-1- 3363	268.7127	-31.8944	-3.225	-1.461	8.176	0.430	1387.10	0.492	
79-2-1- 8900	268.4667	-33.0348	-3.620	-2.534	29.763	0.344	1680.00	0.832	
80-3-2- 7178	269.8741	-32.2297	-4.246	-1.216	35.887	0.049	1047.00	0.876	
80-4-2- 10880	269.4209	-32.6063	-4.100	-1.740	10.348	0.733	2040.10	0.548	
81-3-2- 24224	269.7945	-33.7675	-4.946	-2.545	30.017	0.253	1341.00	0.887	
82-2-3- 24164	270.3955	-32.2755	-4.652	-1.018	13.832	0.285	2357.80	0.631	
83-1-1- 8206	270.5674	-33.2471	-5.253	-1.758	13.159	0.180	1315.10	0.614	
84-4-1- 15036	271.1088	-33.0547	-5.556	-1.351	19.032	0.000	2176.00	0.727	
101-1-1- 20136	263.7159	-29.3984	1.743	-1.622	10.623	0.094	2351.60	0.292	B
102-0-3- 17623	262.5237	-29.4664	2.577	-2.223	25.501	0.152	1322.90	0.593	
102-3-1- 13451	262.6484	-29.7646	2.322	-2.420	12.616	0.290	1093.50	0.554	
102-5-2- 15625	262.7204	-30.2758	1.990	-2.822	24.927	0.139	2197.60	0.587	
102-5-3- 29920	262.9454	-30.2184	1.858	-2.671	33.810	0.586	1348.90	0.642	
103-1-4- 21106	263.1299	-28.1925	2.829	-0.858	23.528	0.310	2380.90	0.630	
103-3-4- 27325	263.1901	-28.5500	2.590	-1.137	10.030	0.662	1777.20	0.463	
104-3-3- 29860	262.2052	-29.1929	2.959	-2.134	12.518	0.142	2064.20	0.572	
104-3-4- 27383	262.1975	-29.3197	2.895	-2.246	20.467	0.575	1984.30	0.651	
105-5-1- 14483	261.1343	-29.5197	3.553	-2.900	7.628	0.682	1636.30	0.334	
105-7-4- 12278	261.2801	-30.0158	3.171	-3.256	25.769	0.356	1604.50	0.739	
106-1-4- 11177	265.1363	-27.0417	1.947	1.043	30.726	0.324	1624.90	0.565	
106-4-1- 8809	264.7175	-27.5637	1.985	0.404	5.775	0.298	1701.50	0.291	
106-4-4- 24841	264.8552	-27.8152	1.748	0.251	24.738	0.453	1073.50	0.785	B
106-4-4- 31028	264.8404	-27.8541	1.739	0.211	17.878	0.535	1623.80	0.687	
106-5-1- 15482	265.0711	-27.6027	1.699	0.531	19.899	0.122	1293.10	0.610	
106-5-1- 26077	264.9651	-27.6713	1.742	0.424	11.974	0.593	2099.10	0.462	
106-5-4- 24760	265.1471	-27.8188	1.527	0.381	25.477	0.093	2524.00	0.679	
106-6-1- 13061	264.6275	-27.9500	1.847	0.032	36.059	0.283	1687.00	0.508	C
107-0-2- 21213	263.4739	-26.7017	3.382	0.578	124.365	0.025	1250.10	0.776	
107-1-2- 24707	263.7571	-26.7073	3.166	0.702	16.090	0.404	2080.40	0.543	
107-3-3- 31150	263.9854	-26.9224	2.878	0.621	19.904	0.591	1309.50	0.754	
107-4-1- 8762	263.3894	-27.1358	3.210	0.166	35.398	0.489	1754.90	0.758	
107-4-4- 23806	263.7192	-27.3873	2.827	0.100	53.574	0.650	1055.00	0.881	
107-5-2- 26345	263.8999	-27.3882	2.692	0.182	14.064	0.197	1710.70	0.576	
107-7-1- 22583	263.8056	-27.5884	2.654	-0.033	8.574	0.075	1635.90	0.415	B
107-7-2- 167	263.9081	-27.6208	2.561	-0.014	9.466	0.220	1616.40	0.455	
108-3-1- 12859	266.2558	-25.8209	1.736	2.604	12.864	0.499	1658.60	0.585	
108-3-1- 27549	266.2520	-25.9237	1.685	2.513	11.375	0.197	888.20	0.504	
108-4-1- 13544	265.9802	-26.1798	1.760	2.169	53.105	0.689	1322.70	0.854	
108-4-1- 23818	265.7825	-26.2489	1.874	2.019	99.504	0.672	2532.60	0.823	
109-4-3- 15519	265.2998	-25.5322	2.621	2.417	17.836	0.417	1365.00	0.686	
112-0-2- 12627	266.7715	-23.3296	2.629	4.995	21.280	0.615	1317.10	0.639	
112-2-2- 25953	266.8246	-23.7485	2.371	4.655	20.012	0.700	1648.60	0.765	
112-5-2- 24472	267.1992	-24.0774	1.907	4.541	23.119	0.676	1011.60	0.558	
112-6-1- 4305	266.7831	-24.1610	2.190	4.279	10.871	0.293	2473.80	0.363	
112-7-3- 14923	267.3655	-24.2420	1.693	4.474	54.797	0.612	1813.50	0.789	
113-1-2- 28239	266.3130	-23.4511	2.926	4.681	23.803	0.066	1967.50	0.768	
113-7-1- 23134	266.3956	-24.3175	2.411	3.967	26.167	0.294	863.60	0.817	

114-3-1- 11753	265.5659	-23.5507	3.458	4.254	18.387	0.076	2044.50	0.728	
114-5-1- 16265	265.5462	-23.9263	3.276	3.919	67.940	0.548	1664.30	0.810	X
117-6-3- 13250	268.0484	-22.5049	2.042	6.293	6.270	0.082	1643.30	0.203	
117-7-1- 12630	268.2245	-22.5131	1.898	6.366	24.160	0.100	1794.70	0.761	
124-1-1- 16687	259.9039	-27.8925	5.362	-2.066	19.173	0.180	1410.20	0.688	
124-7-2- 20832	259.9118	-29.1101	4.664	-3.106	201.882	0.311	2075.30	0.854	P
124-7-3- 21344	260.0548	-28.9748	4.638	-2.925	47.000	0.295	918.50	0.851	

Table 3: The 120 events used for the measurement of the optical depth. The first column gives the identification: field, CCD, quadrant, star number. The time of maximum amplification, t_0 , is shown in the eighth column as (JD-2,450,000). The efficiency, ϵ , used in the optical depth calculation is shown in the ninth column. The final column signals events of special character: P (parallax), X (xallarap or binary lens without caustic), C (caustic binary lens), B (strong blend). Event numbers in the final column preceded by M refer to MACHO events (Popowski et al. 2005) and those preceded by SC refer to OGLE-II events Sumi et al. (2006).

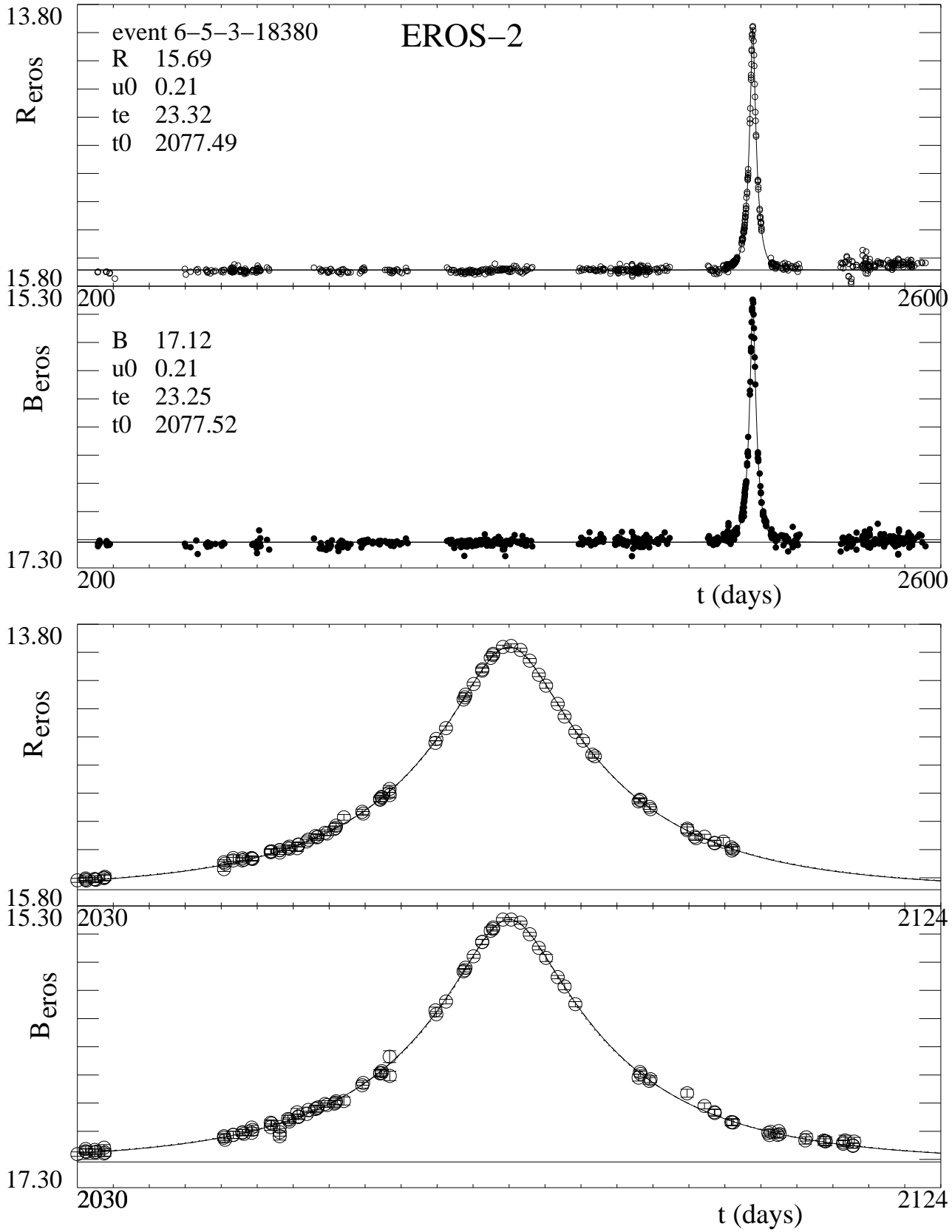


Fig. 21. The light curves of EROS-2 microlensing candidate 6-5-3-18380. Of the 120 candidates, this one has the largest value of $\chi^2(\text{flat}) - \chi^2(\text{microlensing}) = 221600$. The two top panels show R_{eros} and B_{eros} as a function of time (JD-2,450,000). The two bottom panels show a zoom for the time interval $t_0 - 2t_E < t < t_0 + 2t_E$.

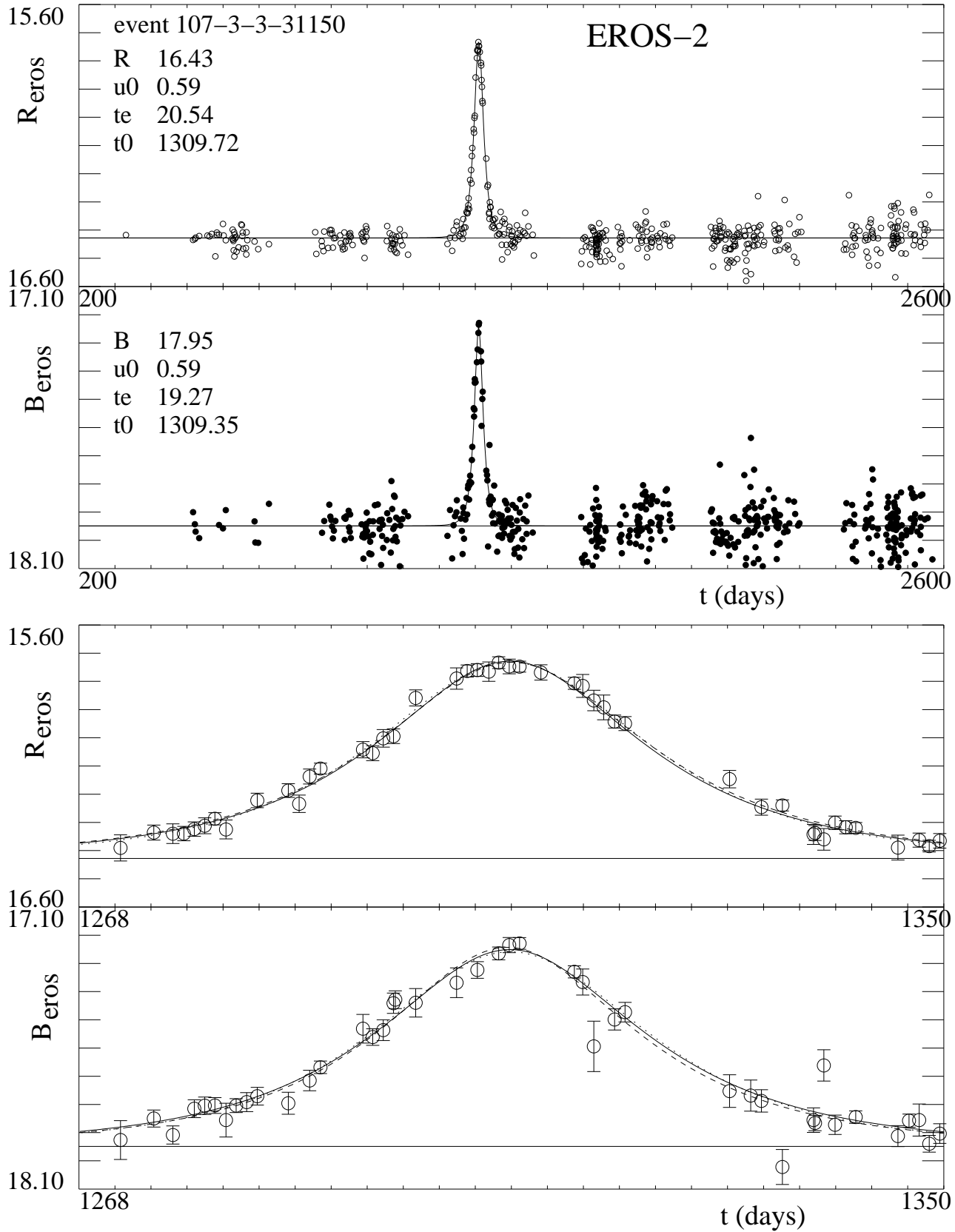


Fig. 22. The light curves of the EROS 2 microlensing candidate 107-3-3-31150. Of the 120 candidates, this one has the median value of $\chi^2(\text{flat}) - \chi^2(\text{microlensing}) = 6810$. The two top panels show R_{eros} and B_{eros} as a function of time (JD-2,450,000). The two bottom panels show a zoom for the time interval $t_0 - 2t_E < t < t_0 + 2t_E$. On the bottom two panels, the solid line is the blend-free simultaneous fit for both colors, the dashed line the blend-free single-color fit, and the dotted line the simultaneous fit with blending.

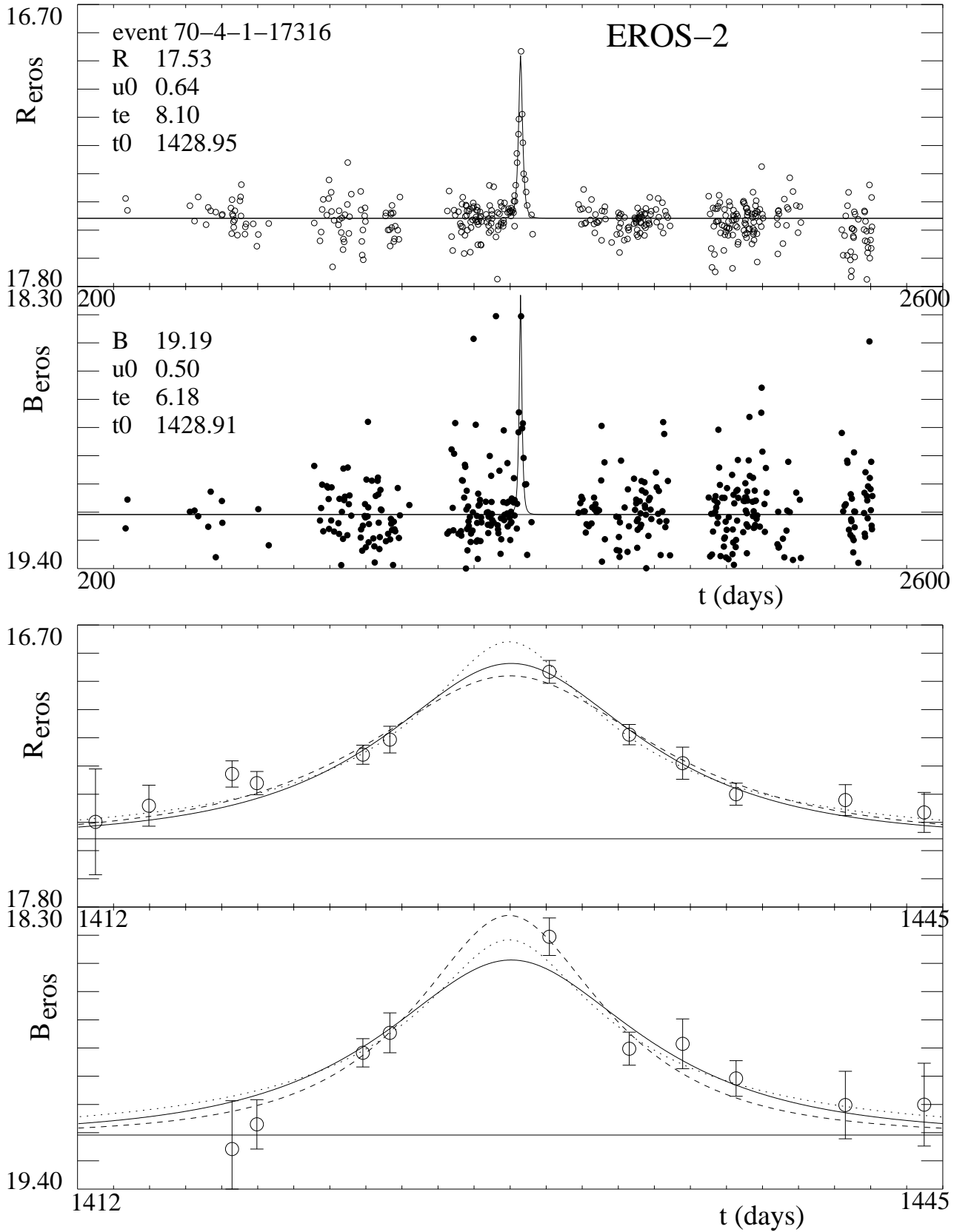


Fig. 23. The light curves of the EROS 2 microlensing candidate 70-4-1-14316. Of the 120 candidates, this one has the smallest value of $\chi^2(\text{flat}) - \chi^2(\text{microlensing}) = 399$. The two top panels show R_{eros} and B_{eros} as a function of time (JD-2,450,000). The two bottom panels show a zoom for the time interval $t_0 - 2t_E < t < t_0 + 2t_E$. On the bottom two panels, the solid line is the blend-free simultaneous fit for both colors, the dashed line the blend-free single-color fit, and the dotted line the simultaneous fit with blending.